J. Fluid Mech. (1985), *vol.* 160, *pp.* 337–367
Printed in Great Britain

Flow along a channel with a time-dependent indentation in one wall: the generation of vorticity waves

By T. J. PEDLEY

Department of Applied Mathematics and Theoretical Physics, University of Cambridge, Silver Street, Cambridge CB3 9EW

AND K. D. STEPHANOFF

Department of Mechanical Engineering and Mechanics, Lehigh University, Bethlehem, PA 18105

(Received 16 October 1984 and in revised form 21 May 1985)

We describe flow-visualization experiments and theory on the two-dimensional unsteady flow of an incompressible fluid in a channel with a time-dependent indentation in one wall. There is steady Poiseuille flow far upstream, and the indentation moves in and out sinusoidally, its retracted position being flush with the wall. The governing parameters are Reynolds number Re, Strouhal number (frequency parameter) St and amplitude parameter ϵ (the maximum fraction of the channel width occupied by the indentation); most of the experiments were performed with $\epsilon \approx 0.4$. For $St \leqslant 0.005$ the flow is quasi-steady throughout the observed range of Re ($360 < Re < 1260$). For $St > 0.005$ a propagating train of waves appears, during every cycle, in the core flow downstream of the indentation, and closed eddies form in the separated flow regions on the walls beneath their crests and above their troughs. Later in the cycle, a second, corotating eddy develops upstream of the first in the same separated-flow region ('eddy doubling'), and, later still, three-dimensional disturbances appear, before being swept away downstream to leave undisturbed parallel flow at the end of the cycle. The longitudinal positions of the wave crests and troughs and of the vortex cores are measured as functions of time for many values of the parameters; they vary with St but not with Re. Our inviscid, long-wavelength, small-amplitude theory predicts the formation of a wavetrain during each cycle, in which the displacement of a core-flow streamline satisfies the linearized Korteweg–de Vries equation downstream of the indentation. The waves owe their existence to the non-zero vorticity gradient in the oncoming flow. Eddy formation and doubling are not described by the theory. The predicted positions of the wave crests and troughs agree well with experiment for the larger values of St used (up to 0.077), but less well for small values. Analysis of the viscous boundary layers indicates that the inviscid theory is self-consistent for sufficiently small time, the time of validity increasing as St increases (for fixed ϵ).

1. Introduction

The motivation for this investigation is to understand incompressible fluid flow through collapsible tubes such as arteries and veins. Earlier laboratory experiments have used rubber tubes, compressed by a local region of high external pressure, in

which large-amplitude, self-excited oscillations are often observed (e.g. Conrad 1969; Ur & Gordon 1970; Bertram 1982). Theoretical models indicate that the dynamics of the oscillations are strongly influenced by the energy dissipation in the flow through the collapsed segment of tube (Katz, Chen & Moreno 1969; Bertram & Pedley 1982; Cancelli & Pedley 1985). At values of the Reynolds number relevant to large blood vessels ($\geqslant 300$, say) most of this dissipation is associated with flow separation from the time-dependent constriction. In the theoretical models the energy dissipation has been estimated on the assumption that the flow is quasi-steady, but this cannot be accurate for the observed oscillations, since the Strouhal number St can be as high as unity (Bertram 1982). Here

$$St = a/\bar{u}_0 T, \tag{1}$$

where a = tube diameter, $\bar{u}_0$ = velocity scale for flow through the uncollapsed tube and T = oscillation period.

In order for an oscillatory flow to be quasi-steady the unsteady inertia terms in the equation of motion must be small compared with both the convective inertia terms and the viscous terms. This requires that two dimensionless parameters are small, St and the viscous frequency parameter $Re\,St$, where the Reynolds number is

$$Re = a\bar{u}_0/\nu \tag{2}$$

and ν is the kinematic viscosity. Since the Strouhal number is not small for self-excited oscillations, and $Re\,St$ is even larger, future theoretical models must incorporate the unsteady fluid dynamics of separated flow.

Sobey (1980, 1982, 1983), Stephanoff, Sobey & Bellhouse (1980) and Savvides & Gerrard (1984) have made experimental and numerical studies of two-dimensional unsteady separated flows in rigid non-uniform channels. The channels in these studies were periodic in the streamwise direction and, except for Sobey (1982), symmetric about the centreplane. The flows were oscillatory, with and without a mean component. These papers show that the flow patterns are quasi-steady throughout the cycle if St and $Re_p\,St$ are very small (where Re_p is peak Reynolds number), and for part of the cycle at larger values of these parameters. Sobey (1983) has proposed $St < 0.2Re_p^{-2}$ as the condition for quasisteadiness throughout the cycle at moderate values of Re_p (< 100).

Bertram & Pedley (1983) investigated impulsively started, but subsequently steady, laminar flow past a single, fixed, slender indentation in one wall of an otherwise parallel-sided channel. Flow-visualization experiments showed that the flow field on the downstream slope of the indentation did not reach a steady state until a dimensionless time $t \geqslant 75$, where $t = \hat{t}\bar{u}_0/a$, $\hat{t}$ is dimensional time, $\bar{u}_0$ is the average velocity in the channel far upstream and a is now the unconstricted channel width. In contrast, pressure measurements showed that the pressure drop along the downstream slope became approximately steady after a dimensionless time in the range $7 \leqslant t \leqslant 10$. These values of t were virtually independent of Reynolds number in the range $500 < Re < 1500$. Inverting them suggests that the pressure drop in oscillatory flow may be quasi-steady if $St \leqslant 0.1$, but that the flow patterns may not be quasi-steady unless $St \leqslant 0.01$.

All the above studies were carried out in channels with fixed walls. In order to model more closely the conditions in an oscillating collapsible tube, we have performed experiments on water flow in a rectangular channel in which a section of one wall is moved in and out (see figure 2). The experiments are still highly idealized, because prescribing the motion of the moving section uncouples the fluid mechanics from the effects of wall elasticity. Moreover, we have followed the previous investigators in

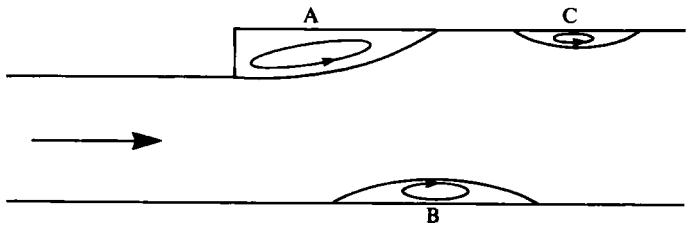

FIGURE 1. Sketch of eddies observed on steady flow over a backward-facing step by Armaly *et al.* (1983).

considering approximately two-dimensional flow, which is probably more relevant than pipe flow to flow in a collapsed tube. The indentation, formed by a thick rubber membrane moulded over a square piston, is pushed sinusoidally into the channel from a flush position. The flow in the channel upstream of the indentation is steady Poiseuille flow. In the experiments very small particles are used to visualize the flow past the indentation.

The flow visualization reveals that there are two flow regimes. If St is less than the critical value of 0.005 (independent of Re in the observed range $360 < Re < 1260$) the flow is quasi-steady in that a single eddy forms on the downstream slope of the indentation and develops and decays in phase with the wall oscillations. If $St \geqslant 0.005$ the flow is no longer quasi-steady; during each cycle a propagating train of waves appears in the core flow downstream of the indentation, and closed eddies form in the separated-flow regions beneath their crests and above their troughs (see figure 5). Later in the cycle, in many cases, second, corotating eddies develop in the same separated-flow regions, upstream of the primary eddies. We refer to this phenomenon as 'eddy doubling'. Still later in the cycle the flow becomes markedly disturbed in all cases; however, all disturbances are swept downstream before the indentation is fully retracted at the end of the cycle. Thus the perturbed flow of one cycle does not interact with the waves and eddies that develop during the next cycle. Some of our observations have already been reported in Stephanoff *et al.* (1983).

Armaly *et al.* (1983) and Sobey (1985) have also observed multiple eddies in asymmetric channel flow. Armaly *et al.* investigated steady flow past a backward-facing step and found, both numerically and from laser-Doppler velocity measurements, that: (*a*) for $Re < 400$ there is a single eddy A in the lee of the step; (*b*) for $400 < Re < 1200$ there is a second eddy B on the plane wall opposite the reattachment point of the first eddy; and (*c*) for $1200 < Re < 2300$ a third eddy C is present further downstream on the wall with the step (see figure 1). Sobey studied oscillatory flow with zero mean velocity past a step, and observed both numerically and experimentally that, during the part of the cycle when the step is backward-facing, a wavetrain forms which is similar to that observed in this study.

A number of authors have presented asymptotic, large-Re theories for laminar unsteady flow in asymmetric channels. The first to consider steady upstream flow past a moving indentation was Smith (1976*b*), who formulated an interactive, nonlinear, unsteady boundary-layer problem for indentations whose length λa, maximum height ϵa ($\epsilon \ll 1$) and Strouhal number St are related to each other and to the Reynolds number Re by

$$\lambda = O(\epsilon^{-\frac{1}{4}}), \quad St = O(\epsilon^{\frac{3}{4}}) \tag{3a}$$

and

$$\epsilon = O(Re^{-\frac{2}{7}}) \tag{3b}$$

The linearized version of Smith's problem ($\epsilon Re^{\frac{3}{7}} \to 0$) was examined thoroughly by Bogdanova & Ryzhov (1983), who showed that Tollmien–Schlichting waves are generated in critical layers of thickness $O(a Re^{-\frac{3}{7}})$ at the wall and propagate downstream. They are associated with waves of displacement on the streamlines in the core. They decay with distance if the frequency of wall oscillation is sufficiently small, but *grow*, leading to instability, if the frequency exceeds a critical value given (in our notation) by $2\pi St Re^{\frac{3}{7}} \approx 4.98$. The wavenumber of the critical waves is $6.39/a Re^{\frac{1}{7}}$. Duck (1985) has demonstrated a similar result for an oscillating indentation in a Blasius boundary layer.

Secomb (1979), on the other hand, considered the large-amplitude limit of Smith's problem ($\epsilon Re^{\frac{3}{7}} \to \infty$), and showed that the equation for the streamline displacement in the core, downstream of the indentation, satisfies a simple evolution equation: the linearized Korteweg–de Vries equation, which clearly exhibits wave propagation. This result has been placed in the wider context of large-amplitude Tollmien–Schlichting waves on general shear flows by Smith & Burggraf (1985). In Stephanoff *et al.* (1983) Secomb's equation was rederived and extended, and was shown to arise as a consequence of neglecting viscosity from the start. The solution of this equation was seen to exhibit several properties in common with the experiments. In the present paper we develop this theory again, but in addition we investigate the conditions in which viscous effects can be neglected.

The outline of the paper is as follows. In §2 the experimental apparatus and flow-visualization technique are described, and the observations (including some data on upstream separation in steady flow) are presented together with such quantitative measurements of the waves and eddies as are possible. In §3 the inviscid theory is developed, and comparisons between theoretical prediction and experimental observation are made. The effect of viscous boundary layers and their separation is also discussed. In §4 there is further discussion, especially of the eddy-doubling phenomenon.

2. Experiments

2.1. *Apparatus and methods*

The experimental system (figure 2) was adapted from that used by Bertram & Pedley (1983). The closed channel is 2.5 m long, 10 mm wide and 100 mm deep; it has rigid walls except for the indentation in one vertical wall. The narrower, horizontal walls are made of perspex, and there are perspex windows (of length 100 mm and 180 mm) in the vertical wall opposite the indentation. The indentation consists of a thick rubber membrane, which begins 1.2 m from the channel inlet, is 165 mm long and over 100 mm deep. It is moulded round an (almost) square piston, 100 × 100 mm, that can move in and out (see figure 2). Ideally, when the piston is fully retracted the membrane is flush with the rest of the plane wall; however slight ridges (< 0.4 mm) were observed where the membrane passed over the ends of the retracted piston.

The piston was driven sinusoidally, and its amplitude and period were adjustable. During the first half of the cycle the piston pushes the membrane into the channel from the flush position. During the second half of the cycle, when the piston is being retracted, the pressure of the water in the channel holds the membrane against the piston and prevents the two sloping parts of the membrane from bulging into the channel. The displacement of the piston from its retracted position was measured with a RM 700 strain-gauge displacement transducer (Shape Industries); the motion of the piston was compared on an oscilloscope screen with sine waves from a waveform

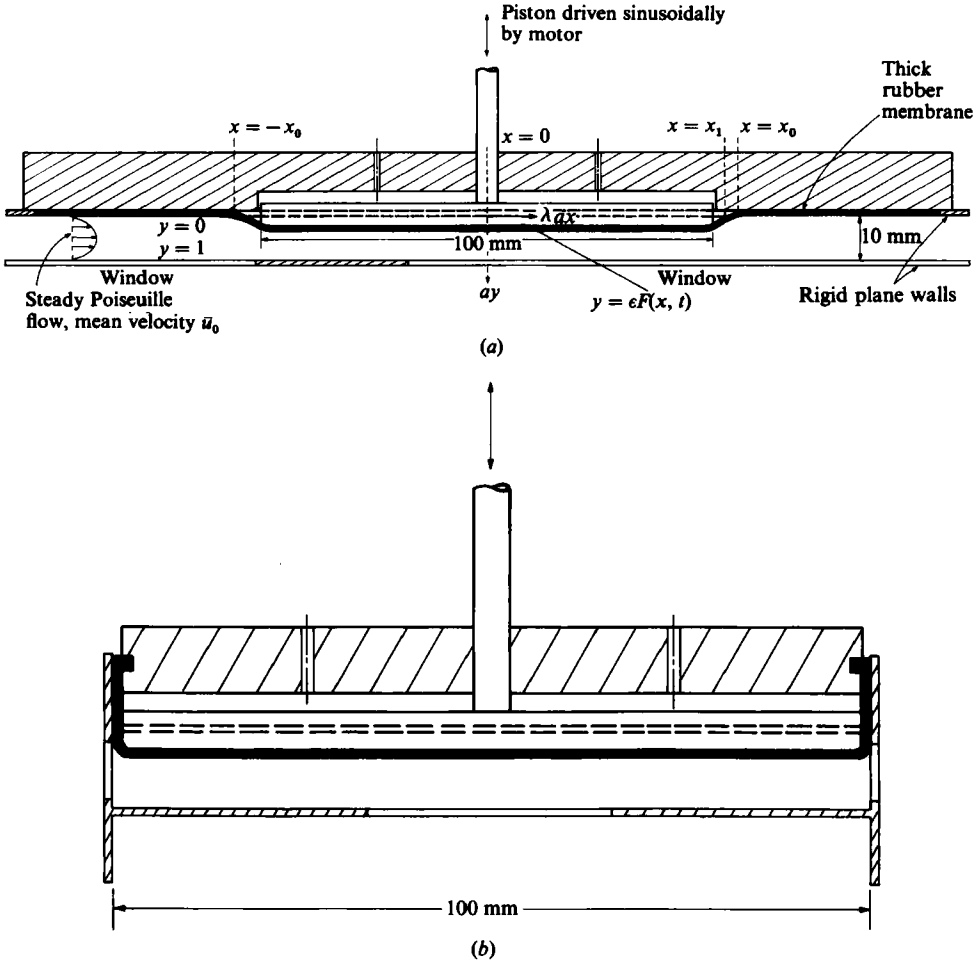

FIGURE 2. (*a*) Sketch of the horizontal channel midplane, showing the section with the moving indentation in one wall, and windows in the opposite wall. Dimensionless variables are also marked (see §3.1). (*b*) Sketch of the cross-section of the channel, showing the membrane wrapped around the piston at the top and bottom.

generator, and was found to be sinusoidal. In each experiment, the amplitude was recorded to the nearest 0.1 mm; it is defined as the maximum protrusion of the indentation, ϵa. The values of ϵ in the unsteady experiments reported here are 0.28, 0.38, 0.57; other values of ϵ were used when the indentation was fixed. The period T of the piston oscillations was measured to within 0.1 s using a Hall-effect switch and a period counter. The lowest period was 2.7 s, and the highest period that was recorded photographically was 15.5 s; longer periods, though, were observed but not photographed.

A Flostat type-V control valve upstream of the channel kept the flow rate of the water entering the channel steady, so that the variations of flow rate caused by the piston motion were confined to the downstream segment of channel. For flow rates in the range 2.88–6.00 l min^{-1} the flow was steady at all frequencies of oscillation, but for flow-rates in the range 6.00–7.59 l min^{-1} the flow could be kept steady only for oscillation periods greater than 10 s. At the higher flow rates and shorter periods

the mean pressure in the system had to be raised both to maintain constant flow rate into the channel and to prevent the membrane from bulging. The steadiness of the flow was checked by observing the weight in a rotameter just upstream of the control valve. The flow rates were measured by making timed collections of the water in a graduated container. The range of average velocities $\bar{u}_0$ in the unconstricted channel corresponding to the above range of flow rates is 0.036–0.126 m s^{-1}. This gives Reynolds numbers in the range $360 \leqslant Re \leqslant 1260$ if the kinematic viscosity is assumed to be 1.00×10^{-6} m^2 s^{-1}. (The temperature of the water varied between 18 °C and 23 °C on different occasions, so that the kinematic viscosity ν varied between 1.06×10^{-6} m^2 s^{-1} and 0.94×10^{-6} m^2 s^{-1}. However, the principal features of the flow prove to be Reynolds-number-independent, so assuming constant ν does not introduce significant errors.) The range of Strouhal numbers St for which records were taken was $0.0052 < St < 0.077$.

We assume that the flow upstream of the indentation is fully-developed Poiseuille flow, because even at $Re = 1260$ the entrance length for steady two-dimensional channel flow is significantly less than 1.2 m (entrance length $= 0.04a\,Re$ (Schlichting 1968, p. 178), equal to approximately 0.5 m in this case). We also assume that the flow near the centreplane of the channel is effectively two-dimensional (see figure 7 and §4).

The fluid motion was made visible with light-reflecting pearl-essence particles known as 'Mearlmaid AA', which remain suspended in the circulating fluid for times in excess of 1 h. The flow was illuminated at the channel centreplane by a collimated beam of light shining through one of the vertical windows. Motion pictures and still photographs of the flow were taken at right angles to the beam of light; the motion pictures were used to obtain general information about the flow and the still photographs were used to obtain detailed information about the unsteady flow at predetermined times in a cycle. The exposure times for the still photographs were either $\frac{1}{8}$ s or $\frac{1}{15}$ s. Both the dimensionless time t_1 between the start of the piston's movement into the channel and the first photograph and the dimensionless time delay Δt between photographs in a cycle were adjustable. These parameters were kept unchanged in most experimental runs of different periods. The field of view of the camera was not wide enough to photograph all the flow that was visible through the perspex windows in the channel. Consequently, to obtain photographs such as those shown in figure 5, the camera was placed at two locations with overlapping fields of view. The left halves of the composite photographs in that figure, which include the downstream end of the constriction, are from one cycle and the right halves from another. In steady flow a few observations were made in the neighbourhood of the upstream end of the indentation.

2.2. *Observations*

Fixed indentation

When the piston is stationary and protruding into the channel, a single eddy is observed along the downstream-sloping wall of the indentation (figure 3*a*). For the smaller Reynolds numbers in the range studied the eddy is confined to the vicinity of the concave corner. As Re is increased for a fixed indentation height, the separation point moves upstream until it reaches the point where the downstream slope begins, where it remains fixed; this is consistent with the observations of Bertram & Pedley (1983). The reattachment point moves downstream at first, until a value of Re is reached at which unsteady oscillations appear in the shear layer between the eddy

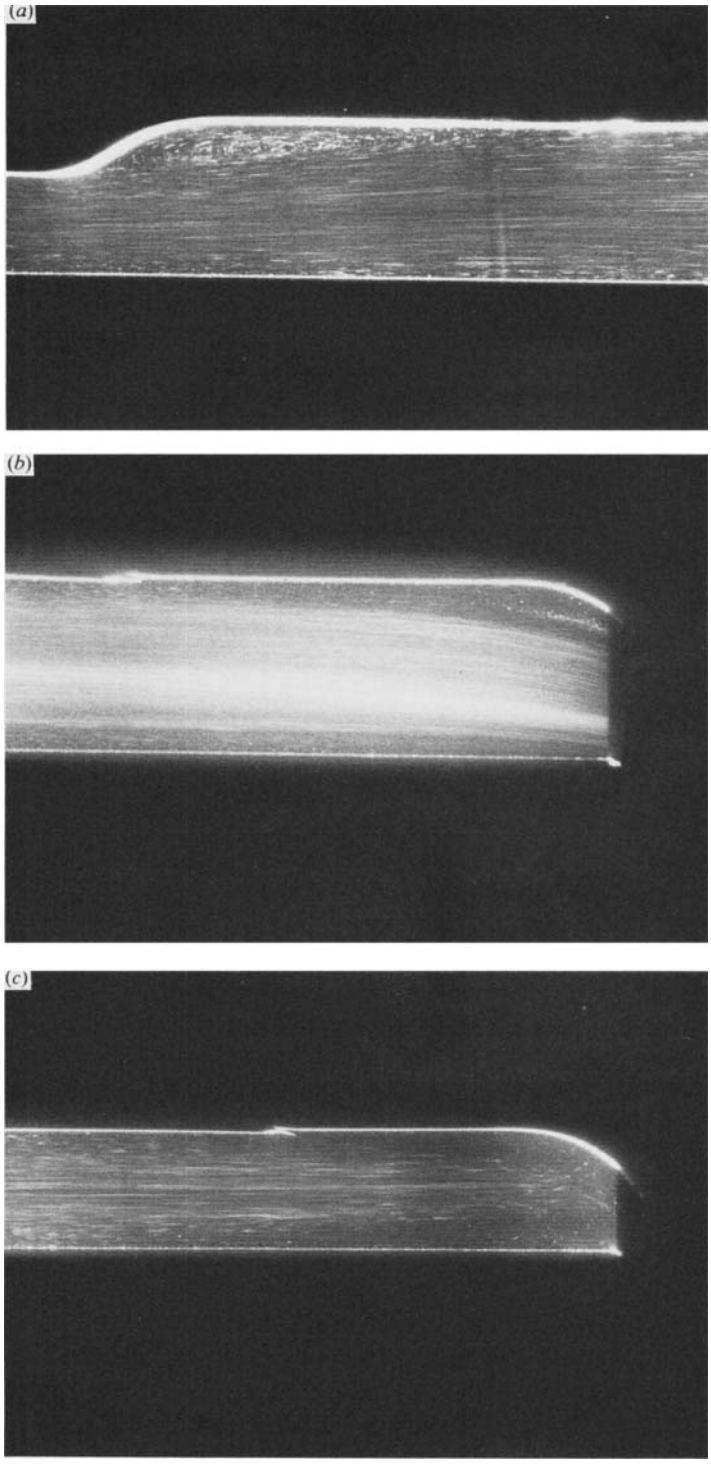

FIGURE 3. (*a*) Photograph of the downstream separated eddy A in steady flow; $\epsilon = 0.35$, $Re = 290$. Because the camera was slightly oblique to the plane of light in this photograph, the membrane appears to be thicker than it actually is. The boundary of the channel is approximately at the centre of the white strip that defines the membrane surface. (*b*) Photograph of an upstream separated eddy in steady flow: $\epsilon = 0.8$, $Re = 1390$. (*c*) Photograph of upstream eddies in steady flow; $\epsilon = 0.8$, $Re = 448$.

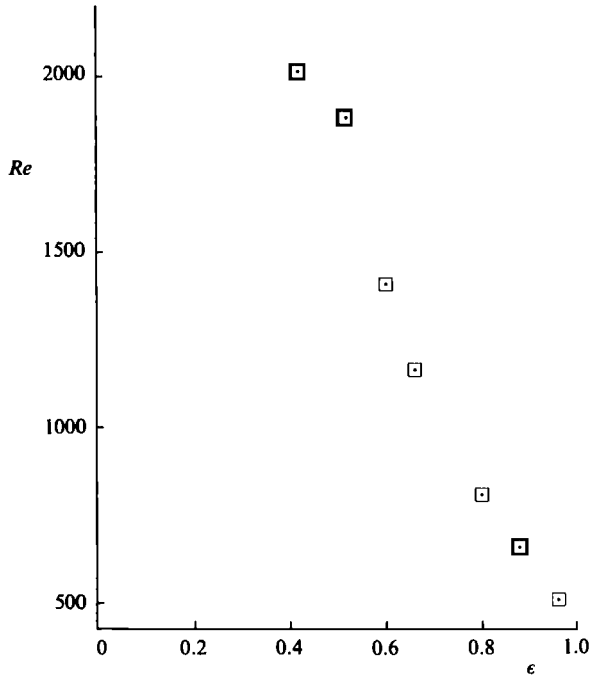

FIGURE 4. The Reynolds number at which upstream separation is first observed, plotted against ϵ.

and the mainstream. Thereafter the mean position of the reattachment point at first moves upstream with increasing *Re* and then remains more or less fixed. This behaviour is consistent with the measurements of Armaly *et al.* (1983). We saw no evidence of the steady second and third eddies (B and C of figure 1) reported by Armaly *et al.* for a sharp-cornered step, with $\epsilon = 0.5$. Such eddies may be present, but could not be observed because the fluid velocities in them are too small. Unsteady eddies which propagate downstream are observed along both the vertical channel walls once the amplitude of shear-layer oscillations has become larger. We interpret these as a feature of the shear-layer instability process and not as part of the basic laminar flow.

We also observe evidence of upstream separation for sufficiently large values of ϵ and *Re*, in that a weak recirculating eddy forms at the concave corner (figure 3*b*). The reattachment point moves downstream as *Re* is increased (for fixed ϵ), until it reaches the convex corner. The separation point is ill-defined, but appears to move slowly upstream as *Re* increases, as predicted by Smith & Duck (1980). In figure 4 the value of *Re* at which upstream separation is first observed is plotted against ϵ.

For very severe constrictions ($\epsilon \geqslant 0.8$) we also observe one, and sometimes two, fixed, clockwise-rotating eddies along the plane wall opposite the upstream slope of the indentation (figure 3*c*). Such eddies were not predicted by Smith & Duck (1980), who found a self-consistent solution on the assumption that the flow on the plane wall remains attached.

Oscillating indentation

In this case there are three dimensionless parameters *St*, *Re* and ϵ; in addition the times at which the observations are made must be specified. The dimensionless time

t is scaled on the period T, so that $t = 0$ when the membrane is flush with the wall and $t = 1$ when it is again flush. The sinusoidal displacement $a\epsilon g(t)$ of the part of the membrane fixed on the piston is then given by

$$g(t) = \tfrac{1}{2}(1 - \cos 2\pi t). \tag{4}$$

Thus the indentation is accelerating into the channel for $0 < t < 0.25$, it is still advancing but decelerating for $0.25 < t < 0.5$, it is accelerating towards the wall for $0.5 < t < 0.75$, and it is decelerating back to its flush position for $0.75 < t < 1$. The flow downstream in the channel is therefore accelerated for $0 < t < 0.25$ and $0.75 < t < 1$, and decelerated for $0.25 < t < 0.75$. All the observations to be reported in this section are made downstream of the indentation.

For very low frequencies, with $St \leqslant 0.005$ and for all ϵ, Re in the range examined, the structure of the observed flow is essentially quasi-steady: except near $t = 0$ and $t = 1$, a single separated eddy A is present on the downstream slope of the indentation, as in figure 3(*a*). Downstream of the eddy the observed streamlines in the main stream fan out and become parallel again (the observed curves are approximately streamlines, since they consist of the union of many short pathlines).

When $St > 0.005$ the flow is not quasi-steady; an example is shown in figure 5, which contains photographs taken at intervals through the cycle during a single run with $\epsilon = 0.38$, $St = 0.038$, $Re = 610$. Sketches of the flow patterns revealed in this figure are presented in figure 6. Near the beginning of the cycle, while the piston is accelerating, a single separated eddy A forms on the sloping wall of the indentation, and the core-flow streamlines remain parallel downstream of it. As t increases, eddy A increases in length. By $t = 0.34$ (figure 5*a*), however, a small upwards wave has appeared on the core-flow streamlines, and a second separated eddy B is beginning to form on the opposite wall, downstream of A. Figures 5(*a–c*) show that this wave and eddy grow and move downstream with time. By $t = 0.48$ (figure 5*c*) there is evidence of a downwards wave and a third eddy C forming on the wall with the indentation, and these too grow and move downstream. A fourth eddy D has appeared on the plane wall by $t = 0.55$ (figure 5*d*), and a fifth E is seen on the other wall by $t = 0.62$ (figure 5*e*). Once they have formed, all the eddies and waves move downstream with a speed that is less than both $\bar{u}_0$ and the speed of propagation of the wave front.

The 'eddy-doubling' phenomenon is observed in figures 5(*c–f*) and 6(*c–f*). Figure 5(*c*) shows that the vortex centre of the clockwise-rotating eddy in the separated-flow region under wave B is located in the downstream half of the region. A second eddy, also rotating in a clockwise sense, subsequently develops in the upstream half, as shown in figures 5(*d–e*), and a double peak appears on the core streamlines in wave B. Wave C and the associated separated region exhibit the same phenomenon a little later in the cycle, but with both eddies rotating in a counterclockwise sense (figure 5*e,f*); the double peak in the core streamlines is more marked in this case. In both cases the upstream eddy grows to a larger size than the primary eddy. Examination of the ciné films and videotapes indicates that the wave in the core flutters just prior to the eddy doubling. The whole process of wave and eddy generation, and eddy doubling, is entirely determinate, occurring at the same time and place during every cycle of a run at fixed values of the governing parameters.

Later in the cycle, the flow becomes disordered (figures 5*g, h*). The particle pathlines have a smeared appearance, symptomatic of significant three-dimensionality, and the eddies break down into turbulence. As the cycle ends, all the disturbances are swept away downstream (figure 5*i*) and the cycle begins again from an undisturbed state.

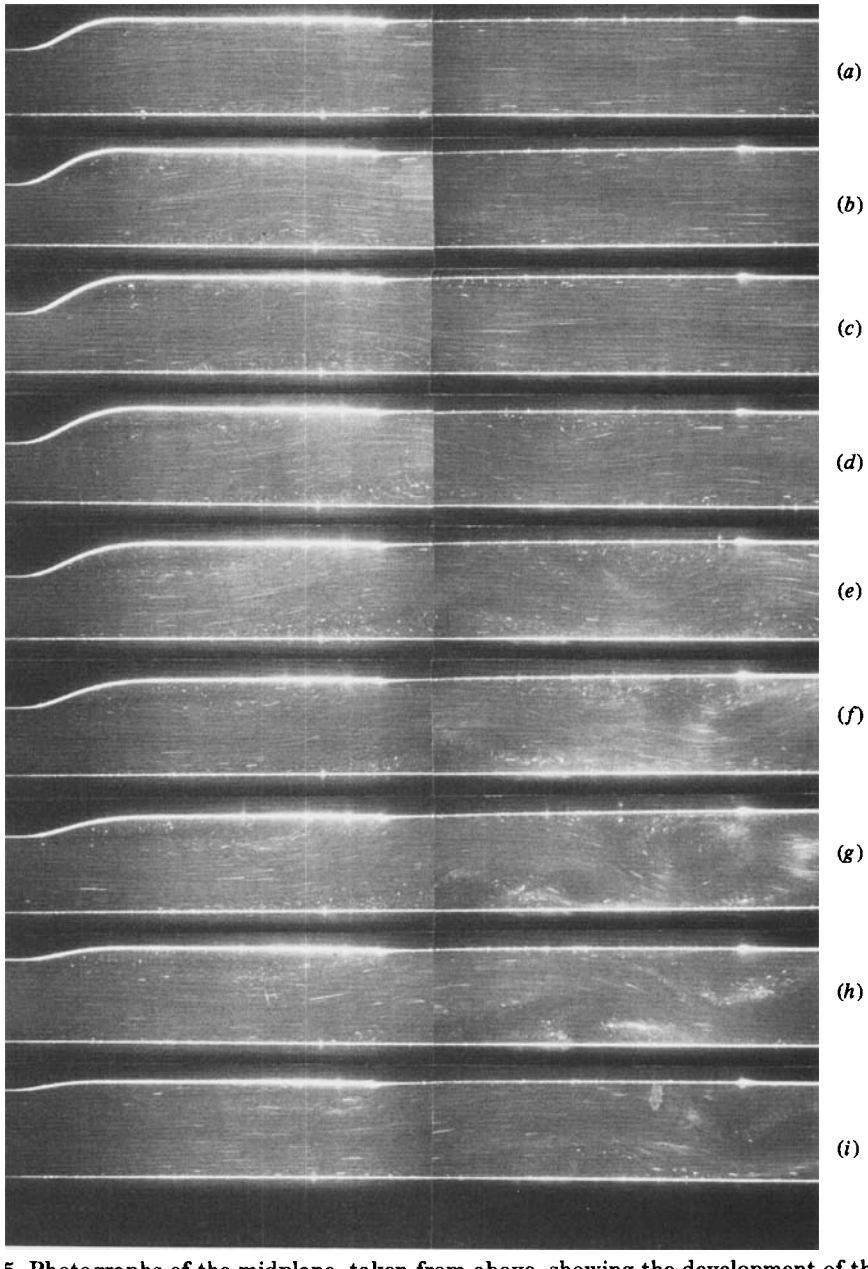

FIGURE 5. Photographs of the midplane, taken from above, showing the development of the flow field downstream of the oscillating indentation. The mean flow is from left to right, and the governing parameters are $Re = 610$, $St = 0.038$, $\epsilon = 0.38$. The dimensionless times at which the photographs were taken are (*a*) $t = 0.34$; (*b*) 0.41; (*c*) 0.48; (*d*) 0.55; (*e*) 0.62; (*f*) 0.69; (*g*) 0.76; (*h*) 0.84; (*i*) 0.91. The second eddy B is first visible in (*b*), the third C in (*c*) and the fourth D in (*d*). Eddy doubling has occurred in (*e*) (eddy B) and (*f*) (eddy C) (from Stephanoff *et al.* 1983).

The fact that the flow pattern is essentially two-dimensional until the final breakdown is demonstrated in figure 7, which contains photographs taken through the downstream window in the vertical wall. Note that the values of the parameters for this run are slightly different from those of figure 5. The pale streak in figure 7 (*a*)

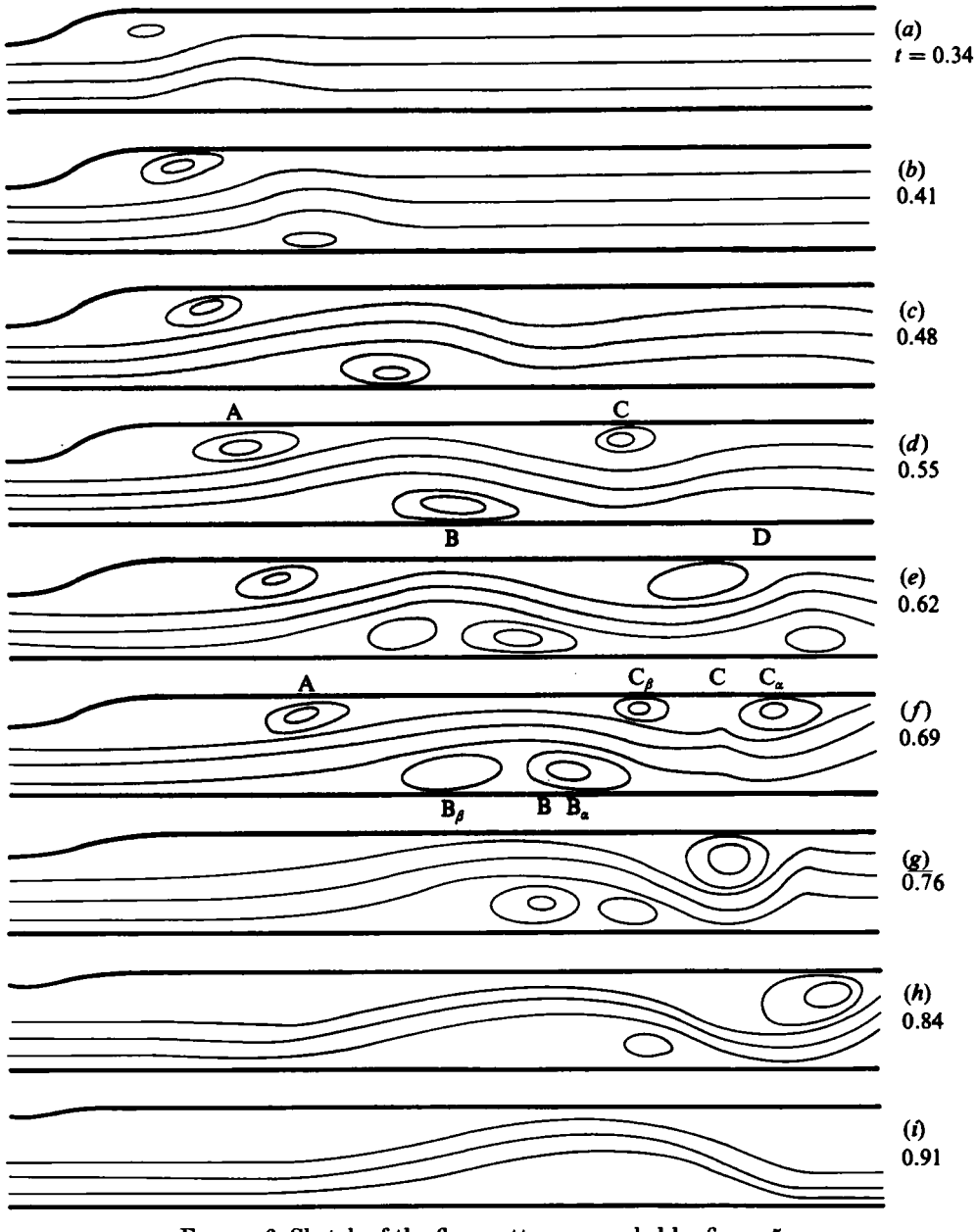

FIGURE 6. Sketch of the flow patterns revealed by figure 5.

represents eddy B just after it has doubled, and appears to correspond to the region between the two parts of eddy B (compare figure 7(*a*) with figure 5(*e*): the bright marks on the wall in figure 5 correspond to the vertical lines in figure 7). Figure 7(*b*) shows the doubled eddy B, now represented by two streaks, with a faint streak opposite the doubled eddy C. Figure 7(*c*) shows further development of these streaks, and the formation of more, while figure 7(*d*) shows clearly the three-dimensional break-up of eddy B, after the beginning of the next cycle.

Qualitatively similar observations of wave and eddy generation, and of eddy

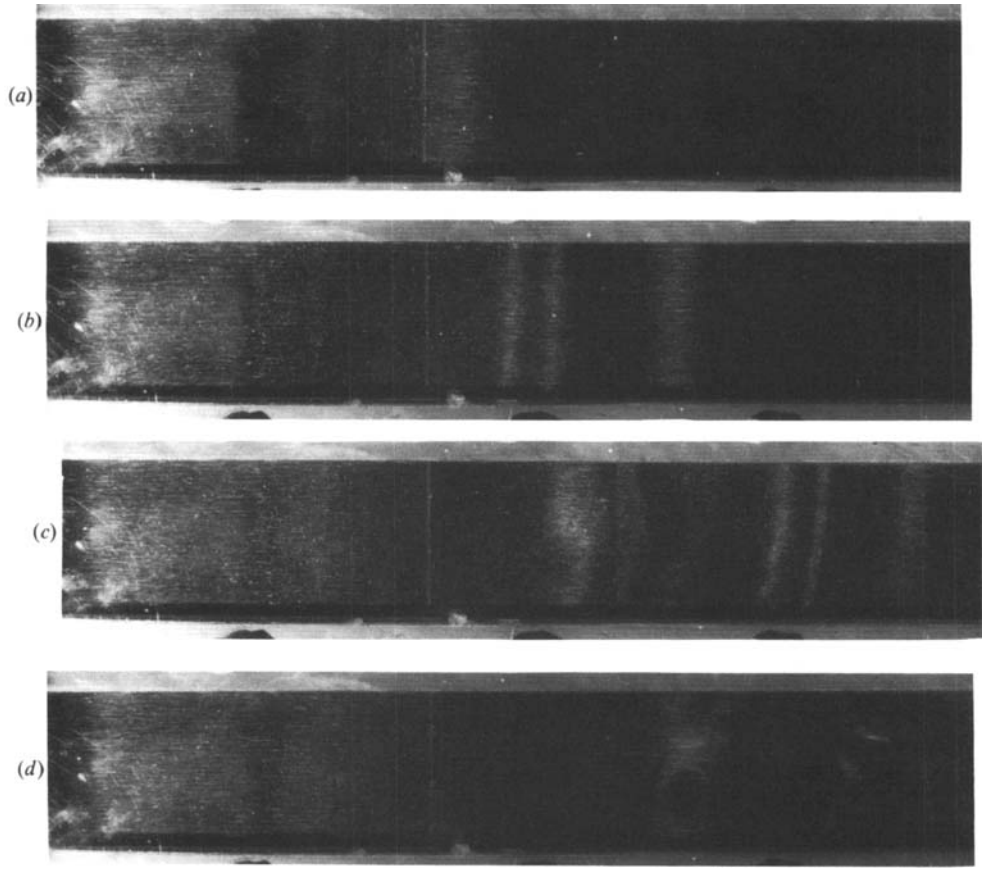

FIGURE 7. Photographs taken from the side, showing the two-dimensional character of the flow during eddy generation and doubling. Note the three-dimensional breakup in (*d*). Governing parameters are $\epsilon = 0.36$, $St = 0.039$, $Re = 615$. Dimensionless times of the photographs: (*a*) 0.60; (*b*) 0.78; (*c*) 0.96; (*d*) 1.14.

doubling, are made in all experiments with $\epsilon = 0.38$ and $St > 0.005$. At smaller amplitude, when $\epsilon = 0.28$, the eddies and waves are generated as before, but eddy doubling is observed in only a few cases. At larger amplitude, with $\epsilon = 0.57$, the generation and doubling processes take place, but few useful photographs could be obtained because the breakdown to turbulence occurs earlier in the cycle, especially at higher values of Re.

2.3. *Quantitative results*

The quantitative data presented in this section were obtained from measurements of the flow patterns; these were made by projecting the photographic negatives onto calibrated, squared paper, and measuring the positions of the principal features of the flow. We let the longitudinal coordinate be $\hat{x}$, and let the middle of the downstream slope of the indentation be at $\hat{x} = \hat{x}_1$ (figure 2). The quantities recorded from each negative are the dimensionless time t and the values of $(\hat{x}-\hat{x}_1)/a$ for the following features.

(i) The points of maximum and minimum displacement of the core streamlines, representing the crests and troughs of the waves. These are recorded as points B, C,

Run	T(s)	St	Re	t_1	Δt	N
			$\epsilon = 0.38$			
30	15.1	0.0052	1265	0.42	0.16	2
29	15.1	0.0056	1173	0.34	0.08	4
27	15.1	0.0062	1068	0.42	0.08	3
24	14.9	0.0071	940	0.34	0.08	5
20	15.0	0.0076	882	0.42	0.08	3
16	15.2	0.0089	737	0.34	0.08	5
28	10.2	0.0091	1075	0.34	0.08	8
11	15.2	0.0095	693	0.34	0.08	6
6	15.3	0.011	588	0.39	0.09	5
21	10.1	0.011	867	0.34	0.08	4
25	10.0	0.011	945	0.34	0.08	4
17	10.1	0.012	800	0.42	0.08	5
1	15.5	0.013	498	0.39	0.09	5
12	10.2	0.014	693	0.42	0.08	6
7	10.0	0.017	592	0.34	0.08	6
26	5.9	0.018	950	0.34	0.08	6
13	7.5	0.019	693	0.42	0.08	5
22	5.9	019	873	0.34	0.08	6
31	8.0	0.019	670	0.40	0.02	18
2	10.1	0.020	485	0.39	0.09	5
18	5.9	0.021	793	0.34	0.08	5
8	7.5	0.022	602	0.42	0.08	4
14	5.9	0.025	693	0.34	0.08	6
3	7.3	0.028	490	0.30	0.09	6
9	5.9	0.030	577	0.34	0.08	7
23	3.9	0.030	855	0.34	0.08	6
4	5.3	0.037	507	0.30	0.09	6
19	2.9	0.043	800	0.34	0.08	7
15	2.9	0.047	722	0.42	0.08	6
10	2.9	0.057	600	0.34	0.08	7
5	2.7	0.077	487	0.43	0.18	3
			$\epsilon = 0.28$			
45	14.9	0.0063	1062	0.42	0.08	3
40	15.1	0.0069	953	0.42	0.08	5
36	14.9	0.0095	702	0.42	0.08	4
44	10.0	0.0096	1033	0.42	0.08	5
42	10.0	0.012	866	0.42	0.08	5
32	15.1	0.013	508	0.42	0.08	5
37	10.0	0.014	703	0.34	0.08	7
43	6.0	0.019	860	0.50	0.08	3
33	10.0	0.020	502	0.34	0.08	6
38	5.9	0.025	687	0.42	0.08	6
41	6.0	0.033	512	0.42	0.08	6
34	5.9	0.034	502	0.34	0.08	6
46	3.0	0.038	880	0.34	0.08	7
39	3.0	0.048	692	0.34	0.08	7
35	3.0	0.067	495	0.34	0.08	7
			$\epsilon = 0.57$			
50	15.2	0.0097	675	0.34	0.08	2
47	15.4	0.013	480	0.34	0.07	2
51	10.0	0.015	680	0.34	0.08	2
48	10.0	0.021	482	0.34	0.08	3
52	6.0	0.025	669	0.34	0.08	2
49	6.0	0.035	477	0.34	0.08	3

TABLE 1. Data for each run for which measurements were made; t_1 is the dimensionless time of the first photograph, Δt is the time step (fraction of a cycle) between photographs and N is the number of photographs taken.

D, etc., corresponding to the eddies B, C, D, etc. marked on figures 6(*d*) or (*f*). Where the crest has a double structure, after eddy doubling, a single stationary point was estimated by eye (figure 6*f*).

(ii) The vortex centres in the eddies. Before eddy doubling the vortex centre in eddy B (for example) is denoted by B_α; after eddy doubling the forward eddy is still denoted B_α and the rearward one is called B_β (figure 6*f*).

It was difficult to measure the exact positions of the maxima and minima of the waves, because the wavelengths are rather long, especially for smaller values of *St*. The largest scatter in the data occurred when the same flow feature (e.g. point C) was measured from both the upstream and the downstream photographs taken at the same value of t. The maximum difference was approximately 3 mm; in such cases the average was recorded. The measurements for a number of experimental runs were checked independently by two observers, and negligible differences were found.

Table 1 lists the governing parameters of the runs from which measurements were taken, and in each case also gives the (dimensionless) time t of the first photograph, the time interval Δt between successive photographs, and the number of photographs taken (simultaneous upstream and downstream photographs of a pair were counted as one). There are three sections to table 1: the first for $\epsilon = 0.38$, the second for $\epsilon = 0.28$ and the third for $\epsilon = 0.57$. In each section the runs are listed in order of increasing *St*; the 'run number' in the first column indicates the chronological order in which the runs were performed, which approximately corresponds to increasing *Re*. Many more photographs were taken in run 31 than in the others, in order to examine the eddy-doubling process in more detail.

The results are presented graphically, with the position $(\hat{x}-\hat{x}_1)/a$ of a feature on the abscissa and time t on the ordinate; most results are for $\epsilon = 0.38$. In figures 8(*a*, *b*) the positions of the first wave crest B and the first trough C are plotted for ten different runs ranging in *St* from 0.0071 to 0.077 and in *Re* from 487 to 945, with $\epsilon = 0.38$. The three runs with $St = 0.011$ are marked by the same symbol, although they have significantly different *Re*. It can be seen that the waves propagate downstream with a roughly constant velocity that decreases as *St* increases, but may not be significantly affected by *Re*.

The theory of §3 suggests that the (dimensionless) lengthscale of the waves should be proportional to $St^{-\frac{1}{3}}$ (cf. (3*a*)), and independent of *Re*. We have therefore replotted the data of figure 8, replacing the abscissa by $x-x_1$, where

$$x = \frac{\hat{x}}{a}(10\,St)^{\frac{1}{3}}; \tag{5}$$

these plots are shown in figure 9. It can be seen that the data for wave crest B collapse into a narrow region for $St \leqslant 0.028$, but for larger values of *St* the points increasingly deviate from this narrow region as t increases above 0.5. The same is true for wave trough C, but with greater spread, and the departure from the common curve appears to occur at $t < 0.5$ if $St \geqslant 0.047$. The data suggest that, for smaller values of *St*, waves B and C propagate with roughly constant phase velocities; the (scaled) velocities are found to be approximately $\mathrm{d}x/\mathrm{d}t = 5.3$ (wave B) and $\mathrm{d}x/\mathrm{d}t = 7.2$ (wave C) if straight lines are drawn through the data points.

The speed of propagation of the wave front is determined by recording the positions of the wave crests B, C, D, E as they first appear in a photographic frame, for every run with $\epsilon = 0.38$. These positions are plotted against the time of the frame in figure 10. This plot does not give a precise estimate of wave-front velocity, because in some

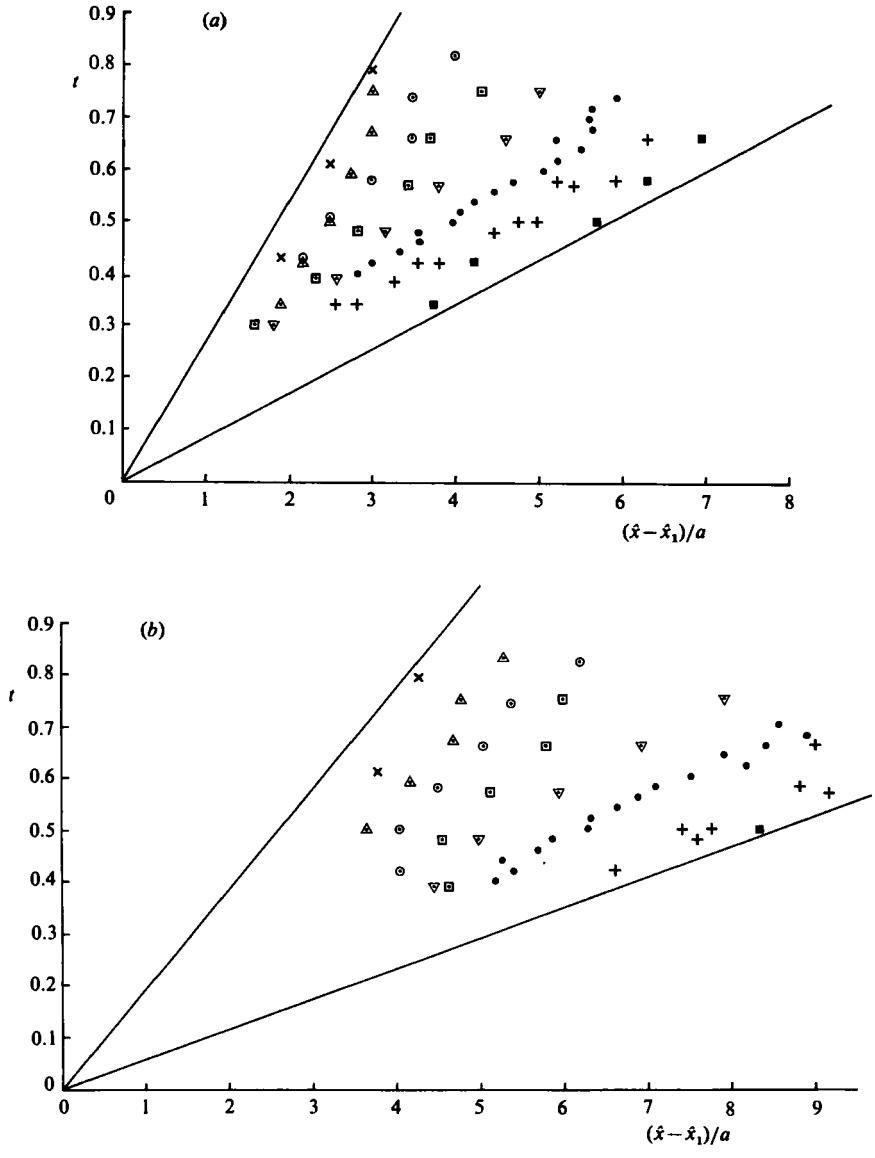

FIGURE 8. Measured positions of wave crest B (*a*) and trough C (*b*) as functions of time. The slopes of the lines drawn give the range of dimensionless phase velocities of the observed waves. Abscissa: dimensionless position $(\hat{x}-\hat{x}_1)/a$; ordinate: dimensionless time t. The symbols correspond to different runs as follows:

Run	24	6, 21, 25	31	3	4	15	10	5
St	0.0071	0.011	0.019	0.028	0.037	0.047	0.057	0.077
Re	940	588 867 945	670	490	507	722	600	487
Symbol	■	+	●	▽	□	○	△	×

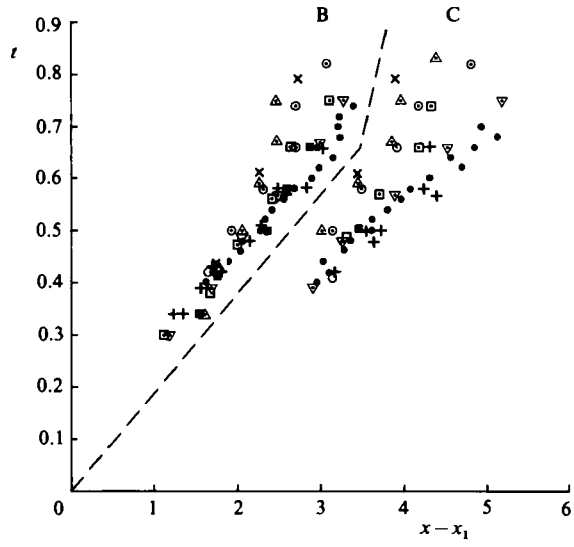

FIGURE 9. The data of figure 8 replotted with $x-x_1$ on the abscissa, scaled according to (5). Symbols as in figure 8; the broken line merely separates C from B.

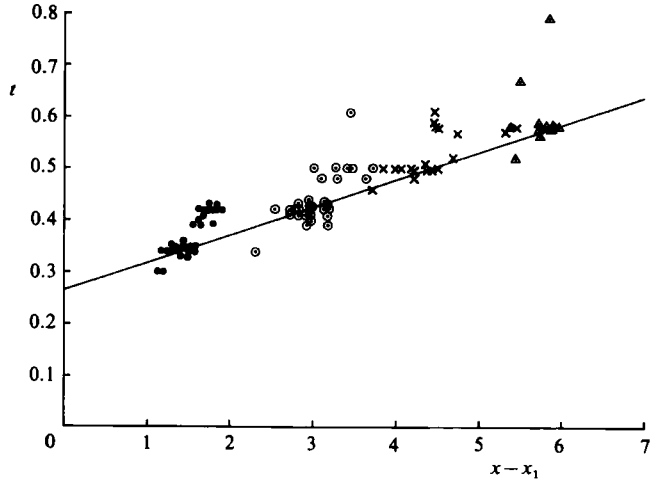

FIGURE 10. Dimensionless times and positions at which the waves in many runs were first observed: ●, wave B; ○, C; ×, D; △, E. The line was drawn by eye through the densest clusters of points.

cases the waves would have appeared before the first frame in the cycle, and in all other cases we know only that the wave became visible sometime between the frame recorded and the previous frame (cf. figure 14). Nevertheless, drawing a straight line through the densest clusters of points gives a value for wave-front velocity, or group velocity, of $\mathrm{d}x/\mathrm{d}t \approx 19$. This is 3.6 times the phase speed of wave B and 2.6 times that of wave C.

To verify the lack of dependence on *Re*, we have in figure 11 plotted the positions of wave crests B, C and D for five different runs with $\epsilon = 0.38$ and with virtually the same value of *St* (0.018–0.020), but with *Re* varying between 485 and 950. No systematic difference can be observed. In addition, points for two runs with

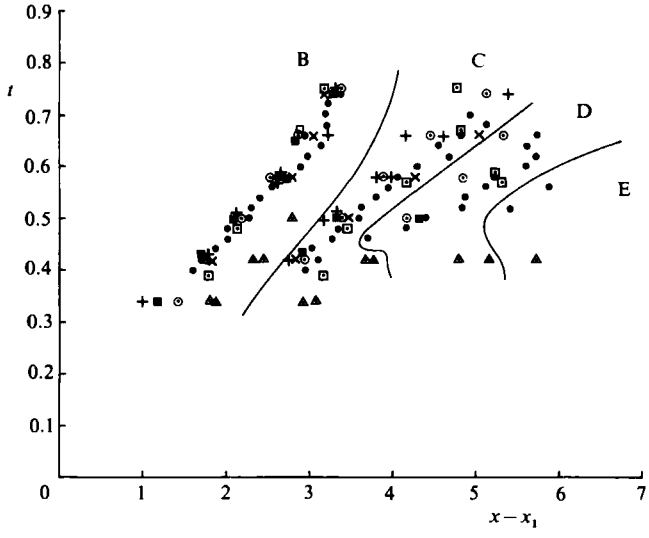

FIGURE 11. The positions of waves B, C, D, E plotted against time for several runs, all with approximately the same value of St, but with different Re and ϵ.

Run	31	22	13	26	2	33	43	48	51
ϵ	0.38	0.38	0.38	0.38	0.38	0.28	0.28	0.57	0.57
St	0.019	0.019	0.019	0.018	0.020	0.020	0.019	0.021	0.015
Re	670	873	693	950	485	502	860	482	680
Symbol	●	○	×	□	■	+	+	△	▲

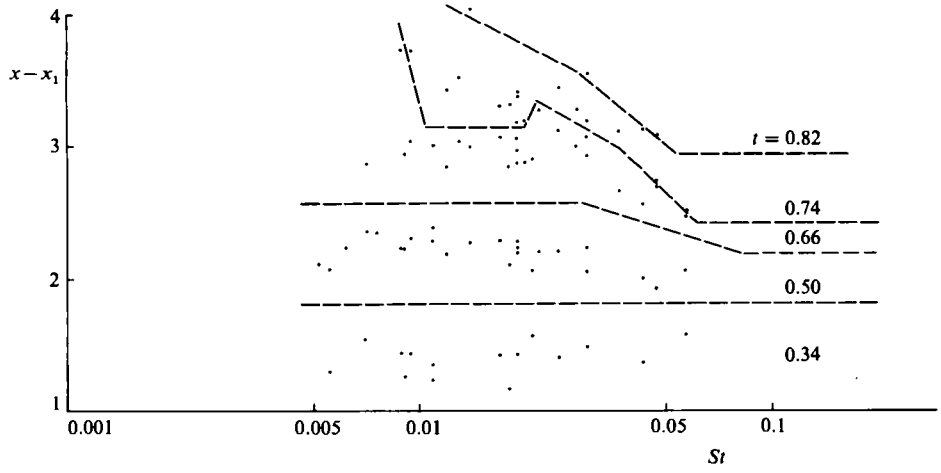

FIGURE 12. Semilog plots of the dimensionless position of wave B against St at different times in the cycle.

comparable values of St (0.015 and 0.021) but with larger amplitude ($\epsilon = 0.57$) are also plotted. The waves are clearly further downstream in this case, but their phase velocity appears to be unchanged. We have also plotted points for the smaller value of ϵ (0.28) and the same St (runs 33 and 43); these points cannot be distinguished from those for $\epsilon = 0.38$.

In figure 12, $x-x_1$ for wave B is plotted against St (on a semilog plot) for different

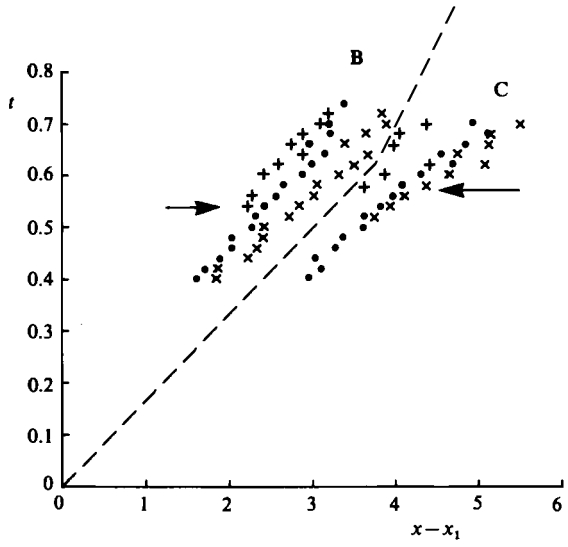

FIGURE 13. Position plotted against time for the wave crest/trough and vortex centres of waves B and C in run 31. The dots represent the wave crest/trough; the diagonal crosses represent either the only vortex centre or the downstream one after eddy doubling; the upright crosses represent the upstream vortex centre after eddy doubling. The arrows indicate the times at which eddy doubling takes place.

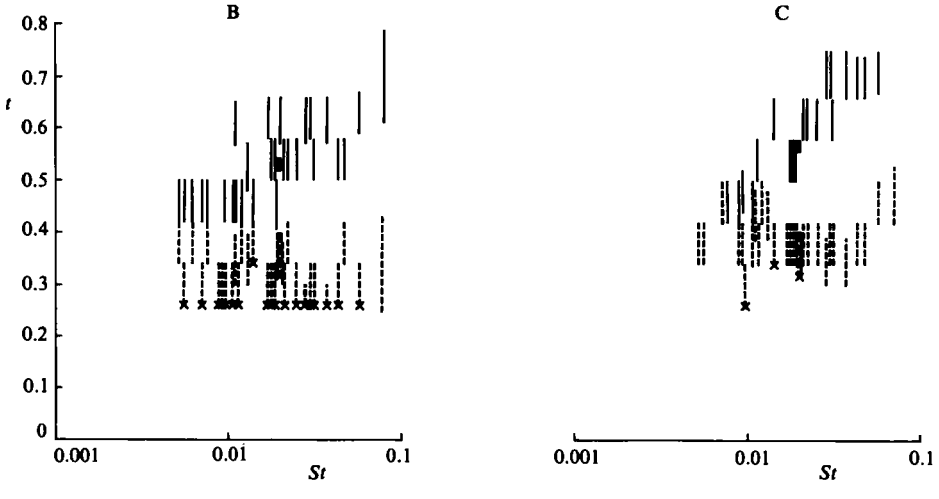

FIGURE 14. Semilog plots showing the times at which waves B and C are first seen (dotted lines) and at which eddy doubling is observed (solid lines), for many runs. Each point is represented by a line indicating the time interval between the last photographic frame in which the flow feature was not seen and the first in which it was. A cross at the bottom of a dotted line shows that the wave was already present in the first frame of the sequence taken, represented by the top. The thick lines represent run 31.

times t, using data from *all* runs with $\epsilon = 0.38$ that include measurements at these times. This figure confirms the impression gained from figure 9 that there is no systematic St-dependence for small times, but that $x - x_1$ falls as St increases above 0.03 when $t \geqslant 0.50$.

Information on eddy doubling, taken from run 31 ($St = 0.019$) is presented in figure 13. The (scaled) positions of the wave crest B and trough C (dots), the vortex centres B_α and C_α (diagonal crosses) and, after doubling, the second vortex centres B_β and C_β (upright crosses) are plotted in this figure. The arrows indicate the times of doubling for the two eddies. Qualitatively similar results, but with many fewer points, were obtained from other runs. As can be seen from figure 13, and as we observed in ciné films, the eddy-doubling process consists of the formation of a second vortex upstream of the first. The propagation speed of the first vortex does not change.

Figure 14 presents data on the Strouhal-number dependence of the times of first appearance and doubling of eddies B and C for $\epsilon = 0.38$. The vertical lines in the figure represent the time interval, between successive frames, during which the generation or doubling process has taken place. The short thick lines represent run 31 in which the interval between successive frames is shorter. There appears to be no systematic St-dependence in the (dimensionless) time at which either eddy is first seen (C of course arising later than B), but there is a tendency for the time of eddy doubling to increase with St. This increase is sharper for eddy C than for eddy B.

3. Theory

3.1. *Inviscid theory*

In the experiments described above the longest oscillation period was approximately 15 s, while the viscous diffusion time a^2/ν is of the order of 100 s. Thus one might expect that the flow in the core of the channel, far from the walls, would be governed by inviscid dynamics and that a large-Re asymptotic theory may be applicable; we outline such a theory in this subsection. The neglect of viscosity is equivalent to assuming that the boundary layers at the walls, and the closed eddies themselves, are passive structures, generated in response to core-flow dynamics but not affecting those dynamics. There are many cases in which such an assumption is false (Smith 1982), but the analysis of §3.3 indicates that it is self-consistent in the present context at sufficiently large values of St for all t in $0 < t < 1$, and for sufficiently small t at all St. Important physical features that are included in the inviscid theory are unsteadiness, since the observed flow is not quasi-steady, and a non-zero cross-stream pressure gradient to account for the observed streamline curvature. As shown by Stephanoff *et al.* (1983), this theory predicts the generation of waves, and in §3.2 the predicted positions of the wave crests are shown to agree well with those measured experimentally for larger values of St.

The present theory is further simplified by assuming that the disturbances to the oncoming flow have small amplitude, low frequency and long wavelength. That is, $\epsilon \ll 1$, $St \ll 1$ and $\lambda \gg 1$, where λa is the longitudinal lengthscale of the waves (cf. (3a)). We introduce dimensionless variables (t, x, y, u, v, p) as follows: time Tt, coordinates $a(\lambda x, y)$ (see figure 2), velocity components $\bar{u}_0(u, v/\lambda)$, pressure $\rho\bar{u}_0^2 p$, where ρ = fluid density. The channel boundaries are taken to be at $y = 1$ and at $y = \epsilon F(x, t)$, where $F = 0$ for $|x| \geqslant x_0$ (figure 2). We require steady Poiseuille flow far upstream; that is,

$$u \sim U_0(y) \equiv 6y(1-y), \quad p \sim \frac{-12\lambda x}{Re} \tag{6}$$

as $x \to -\infty$. In terms of the above variables, the two-dimensional Navier–Stokes equations are as follows, where a suffix represents partial differentiation:

$$u_x + v_y = 0, \tag{7}$$

$$\lambda St\, u_t + uu_x + vu_y = -p_x + \lambda Re^{-1}(u_{yy} + \lambda^{-2}u_{xx}), \tag{8}$$

$$\lambda^{-1} St\, v_t + \lambda^{-2}(uv_x + vv_y) = -p_y + \lambda^{-1} Re^{-1}(v_{yy} + \lambda^{-2}v_{xx}). \tag{9}$$

The kinematic boundary conditions, to be satisfied by inviscid flow, are

$$\left.\begin{aligned} v &= 0 \quad \text{on } y = 1, \\ v &= \epsilon(uF_x + \lambda St\, F_t) \quad \text{on } y = \epsilon F(x,t). \end{aligned}\right\} \tag{10}$$

The no-slip condition for a viscous fluid gives $u = 0$ on $y = 1$ and $y = \epsilon F$.

We assume $\lambda \ll Re$, so that viscosity is negligible in the core. We also assume $\epsilon \ll 1$ and expand the dependent variables in powers of ϵ, so that the leading term in u is the undisturbed flow $U_0(y)$. We shall further take $\lambda St \ll 1$, so that the x-momentum equation (8) is quasi-steady to leading order. Combined with the long-wavelength approximation, this means (a) that the $O(\epsilon)$ term in the expansion for the pressure is identically zero (to avoid singularities on the walls) and (b) that the $O(\epsilon)$ terms in u and v represent nothing but a sideways displacement of the oncoming streamlines. Thus we have

$$\left.\begin{aligned} u &= U_0(y) + \epsilon A(x,t)\, U_0'(y) + \epsilon^2 u_2(x,y,t) + \dots, \\ v &= -\epsilon A_x(x,t)\, U_0(y) + \epsilon^2 v_2(x,y,t) + \dots, \\ p &= \epsilon^2 p_2(x,y,t) + \dots \frac{-12\lambda x}{Re}, \end{aligned}\right\} \tag{11}$$

where $A(x,t)$ is the as yet unknown displacement function. The leading term in the y-momentum equation (9) gives

$$p_2 = P(x,t) + \lambda^{-2}\epsilon^{-1} A_{xx} \int_0^y U_0^2(y')\, dy', \tag{12}$$

showing that the transverse pressure gradient is proportional to the curvature A_{xx} of the displaced streamlines; the function $P(x,t)$ is unknown. The cross-stream pressure gradient will be important at this order if we take $\lambda = O(\epsilon^{-\frac{1}{2}})$, as recognized by Smith (1976b). Finally, the $O(\epsilon^2)$ term in (8) gives

$$\lambda St\, \epsilon^{-1} A_t\, U_0' + AA_x\, U_0'^2 + U_0\, u_{2x} - AA_x\, U_0\, U_0'' + U_0' v_2 = -P_x - \lambda^{-2}\epsilon^{-1} A_{xxx} \int_0^y U_0^2(y')\, dy'. \tag{13}$$

Again, for unsteadiness to be important, the first term should be $O(1)$, and we therefore set $St = O(\epsilon\lambda^{-1}) = O(\epsilon^{\frac{3}{2}})$. These relationships between St, λ and ϵ are the same as those given by ($3a$).

In our experiments, the parameters ϵ and St are specified, while the lengthscale λ of the waves is not. In accordance with the above scaling, we arbitrarily choose

$$\lambda = (10\, St)^{-\frac{1}{3}} \tag{14}$$

(cf. (5)). We also introduce the $O(1)$ parameter

$$\epsilon_1 = 30\lambda^2\epsilon = 30\epsilon(10\, St)^{-\frac{2}{3}}, \tag{15}$$

so $\lambda^{-2}\epsilon^{-1} = 30/\epsilon_1$ and $\lambda St\, \epsilon^{-1} = 3/\epsilon_1$.

Equation (13) can be integrated with respect to y, and a function of integration is introduced that accounts for the variation in flow rate required by conservation of mass. However, this variation in flow rate does not influence $A(x,t)$. Assuming that the kinematic boundary conditions (10) may be applied, we can without integration evaluate (13) at the two boundaries. On the upper boundary $y = 1$ we obtain

$$P_x = 36\left(\frac{1}{2\epsilon_1} A_t - AA_x - \frac{1}{\epsilon_1} A_{xxx}\right), \tag{16}$$

with a similar equation on $y = \epsilon F$. Eliminating P then yields a single partial differential equation for $A(x,t)$:

$$A_{xxx} - A_t = \tfrac{1}{2}F_t + \epsilon_1(FF_x + AF_x + FA_x). \tag{17}$$

Smith & Duck (1980) derived the steady equation corresponding to this; Secomb (1979) derived the unsteady equation, but in the limit $\epsilon_1 \to 0$. Equation (17) is the key equation from which predictions of $A(x,t)$ will be made in the next section.

Where $F \equiv 0$, in the upstream and downstream regions of the channel, (17) reduces to the linearized Korteweg–de Vries (KdV) equation. Its solution consists of the superposition of downstream-propagating waves whose group velocity is three times the phase velocity, in qualitative agreement with our observations of the wave front.

It is interesting to note that the nonlinear term AA_x, present in (13) and (16), is absent in the final equation (17), because its coefficient in (13), $U_0'^2$, has the same value on both $y = 0$ and $y = 1$. The unsteady term A_t does not cancel out in a similar way, because its coefficient U_0' has different values on the two walls, i.e. the vorticity in the basic flow varies cross the channel. This is revealed more clearly from the vorticity equation: (17) can be derived by integrating the $O(\epsilon^2)$ term in the vorticity equation across the channel, and the A_t term comes from the integral of $\partial/\partial t$ of the $O(\epsilon)$ vorticity $-AU_0''$. Thus the waves owe their existence to the non-zero vorticity gradient in the basic flow, and we therefore call them 'vorticity waves'. They are physically similar to Rossby waves in the atmosphere, albeit on a much smaller scale.

The present waves can also be described as Tollmien–Schlichting waves of sufficiently large amplitude that viscous effects have become negligible, a limit analysed thoroughly by Smith & Burggraf (1985), principally in the context of boundary-layer instability. The Tollmien–Schlichting scaling (3*a*, *b*) suggests that this limit can be written $h = \epsilon Re^{\frac{1}{3}} \to \infty$; a corollary is that $St\, Re^{\frac{1}{3}} = O(h^{\frac{1}{2}}) \to \infty$, so that it can also be said that these are high-frequency Tollmien–Schlichting waves.

3.2. *Results and comparison with experiment*

In order to make quantitative comparison with experiment we have performed numerical integrations of (17), with the initial condition of zero disturbance to Poiseuille flow: $A(x,0) = 0$. This condition is based on the observation that all disturbances are swept away at the end of the cycle. If the wavelength is very long and the streamline-curvature term A_{xxx} is neglected in (17), the solution is $A = -\frac{1}{2}F$ (Smith 1976*a*). It is therefore convenient to rewrite the equation in terms of the new dependent variable

$$B(x,t) = A(x,t) + \tfrac{1}{2}F(x,t). \tag{18}$$

An explicit method was used for the integration of the equation, and for numerical stability the time step Δt was required to be less than a given multiple of $(\Delta x)^3$, where Δx is the x-step. Since the linearized KdV equation allows the propagation of waves with every wave number k, at phase speed k^2, it is necessary to suppress waves reflected from the ends of a finite x-domain; this was done according to the recipe

of Vliegenthart (1971). With these precautions, however, the integration was straightforward and stable.

Any sufficiently smooth function $F(x,t)$ can be used in (17), but to model the experiments we considered only separable functions $F(x,t) = f(x)\,g(t)$, where $g(t) = \frac{1}{2}(1-\cos 2\pi t)$ as in (4). The experimental indentation is long, and if $f(x)$ was defined to represent its shape accurately the computation time became excessive. Observation indicates that the disturbances introduced at the upstream end of the indentation do not perturb the flow at the downstream end. We therefore assumed an indentation shape in the form of a single step, and took $B = 0$ as the upstream boundary condition. In dimensional terms we chose

$$f(\hat{x}) = \tfrac{1}{2}\{1-\tanh[\hat{\alpha}(\hat{x}-\hat{x}_1)]\},$$

where $\hat{x}_1$ is the midpoint of the downstream slope and $\hat{\alpha}$ is a constant, which we set equal to 0.414 mm^{-1}. This gives $f = 0.01$ where $\hat{x}-\hat{x}_1 = 6.4$ mm, which is in good agreement with the real indentation. In dimensionless terms the equation for f is

$$f(x) = \tfrac{1}{2}\{1-\tanh[\alpha(x-x_1)]\}, \tag{19}$$

where

$$\alpha = \hat{\alpha}a(10\,St)^{-\frac{1}{2}}, \quad \hat{\alpha}a = 4.14. \tag{20}$$

The numerical problem now has two independent parameters ϵ_1 and α. However, in modelling the experiments at given values of ϵ and $\hat{\alpha}a$, they are both determined by the value of St ((15) and (20)), and are related by

$$\alpha^2 = \frac{(\hat{\alpha}a)^2\epsilon_1}{30\epsilon} = 0.57\,\frac{\epsilon_1}{\epsilon}. \tag{21}$$

When $\epsilon = 0.38$ the extreme values of St in the experiments, 0.0052 and 0.077, correspond to $\alpha = 11.1$, $\epsilon_1 = 82.0$ and $\alpha = 4.5$, $\epsilon_1 = 13.6$ respectively. Sufficient accuracy in the numerical integration was achieved by taking $\Delta x = 0.13/\alpha^{0.43}$, and stability was ensured by taking $\Delta t = \Delta x^3/(4+\epsilon_1\Delta x^2)$. In all cases the range of $x-x_1$ used in the calculation was $-6 < x-x_1 < 15$.

The first comparisons between numerical solutions and experiment were made for fairly large values of St, runs 10 ($St = 0.057$) and 4 ($St = 0.037$), because less computer time is required for smaller values of α. The results were plotted in Stephanoff *et al.* (1983) and in Pedley (1984) respectively, and are reproduced here. Figure 15 shows the predicted variation of A with x at different times t during a cycle for run 10. A positive value of A corresponds to an upward displacement of streamlines in the channel (see figures 2, 5). Waves are generated, grow and propagate downstream in a manner that is qualitatively the same as observed experimentally. If we suppose that a wave crest (or trough) is not visible until $|A| > 0.02$, then figure 15 shows that no waves would be seen initially; by $t = 0.2$ a single crest (wave B of figure 6) would just be visible; by $t = 0.4$ the first trough (wave C) would be seen, and the next crest (wave D) would appear between $t = 0.5$ and $t = 0.6$. Qualitatively similar waveforms are obtained numerically for all values of St in the range covered by the experiments.

The maxima and minima of the predicted waveform that correspond to waves B, C, D, E in the experiments are marked in figure 15. Their positions are plotted as functions of t in figure 16 (*a*), together with the observations from run 10; the curves are theoretical, the points experimental. The corresponding results for run 4 are shown in figure 16 (*b*). Each theoretical curve begins at the time when the magnitude of the relevant maximum or minimum equals 0.02. In the case of run 10, the agreement between theory and experiment for wave B is excellent, for wave C it is reasonable,

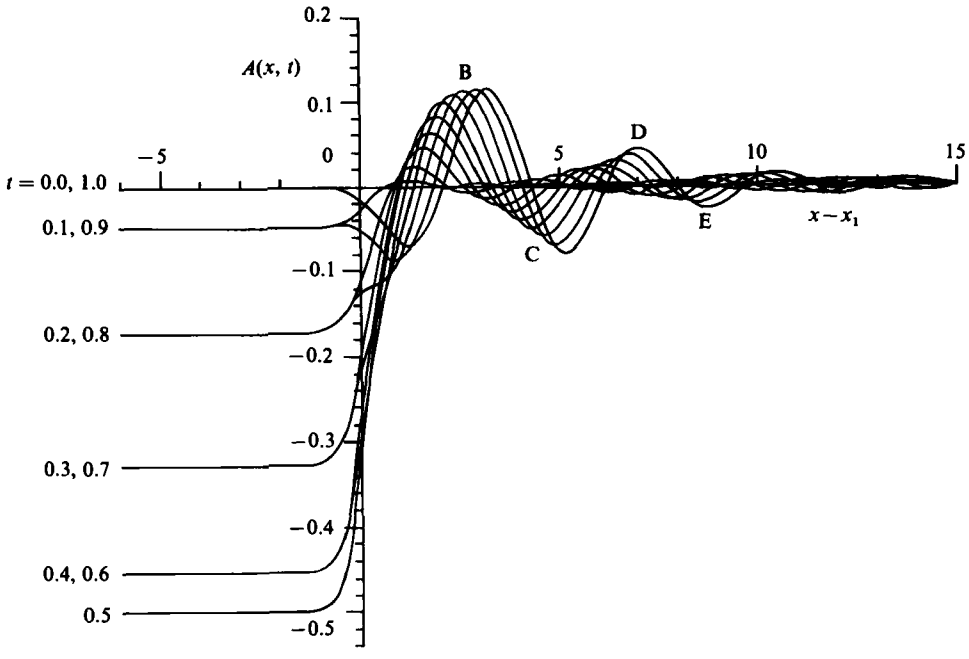

FIGURE 15. Graphs of A against $x-x_1$ at different times t during a cycle, computed from (17), with $F(x,t)$ given by the product of (4) and (19) and with $\epsilon_1 = 16.6$, corresponding to run 10.

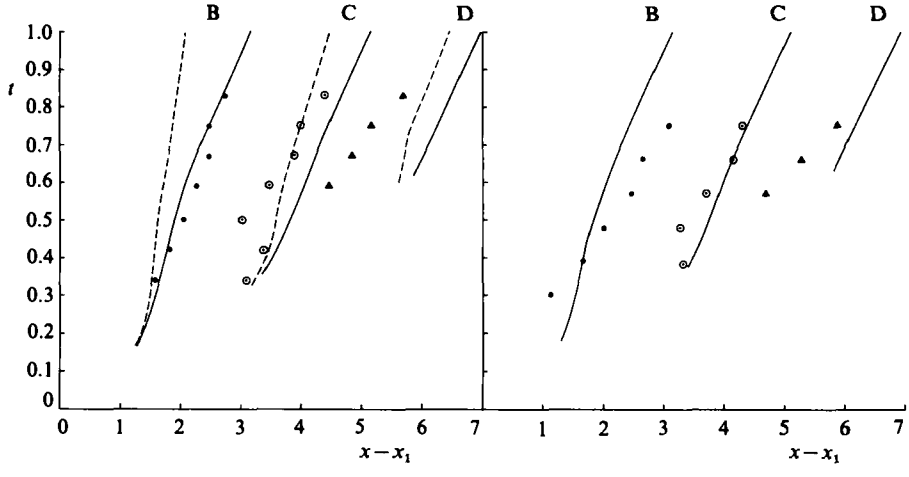

FIGURE 16. Predicted and measured positions of the wave crests and troughs, plotted against time, for (*a*) run 10, $St = 0.057, \epsilon_1 = 16.6$; (*b*) run 4, $St = 0.037, \epsilon_1 = 21.7$. The solid curves are theoretical, beginning at the time when the magnitude of the relevant maximum or minimum of A equals 0.02. The points are experimental: ●, wave B; ○, C; △, D. The broken curves in (*a*) represent the predicted positions when $g(t) = \pi^2 t^2$.

but for wave D the theory significantly overestimates the downstream distance travelled by the wave, although the slope of the curve (the speed of propagation) is reasonably well predicted. In run 4, agreement is best for wave C, but is not bad for waves B and D. The actual wave speed $\mathrm{d}x/\mathrm{d}t$ is a little greater than predicted in this case.

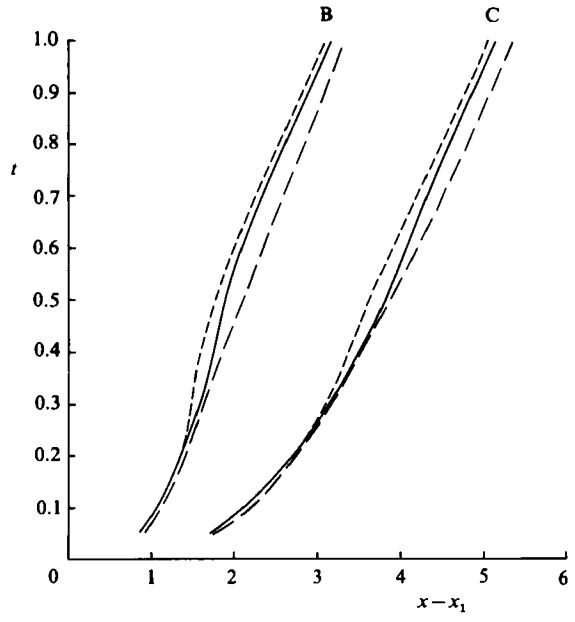

FIGURE 17. Effect of varying ϵ_1 (i.e. St) on the predicted positions of waves B and C: — — —, $\epsilon_1 = 5.9$ ($St = 0.265$); ——, 16.6 (0.057); – – –, 32.3 (0.021).

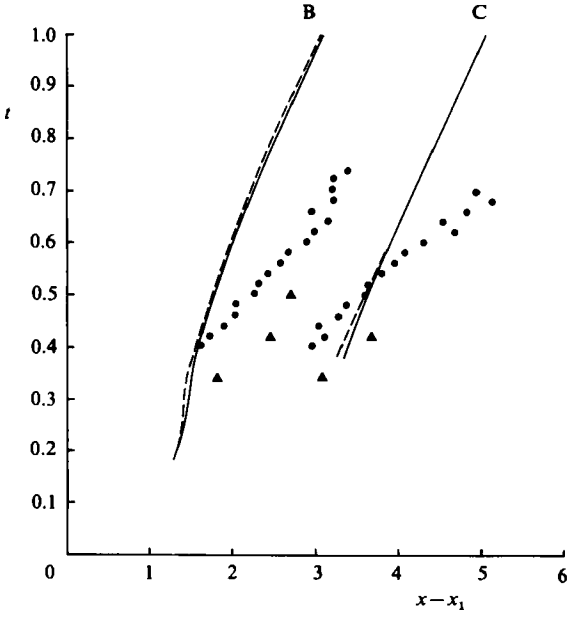

FIGURE 18. Predicted and measured positions of wave crest B and trough C plotted against time. Solid curves: theory for $\epsilon = 0.38$, $St = 0.021$ ($\epsilon_1 = 32.3$); broken curves: theory for $\epsilon = 0.57$, $St = 0.021$ ($\epsilon_1 = 49$). Experimental points: ●, run 31 ($\epsilon = 0.38$, $St = 0.019$), ▲, run 48 ($\epsilon = 0.57$, $St = 0.021$).

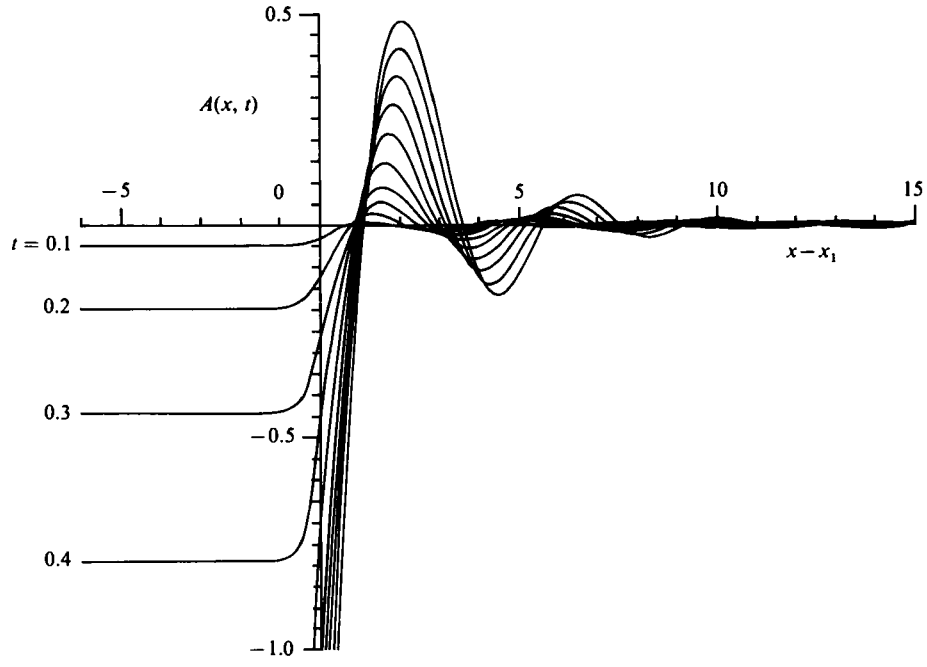

FIGURE 19. As figure 15, but with $g(t) = \pi^2 t^2$.

Agreement between theory and experiment becomes worse at lower values of St. Figure 9 shows that the experimental curves move to the *right* as St decreases (for $t \geqslant 0.45$), representing a larger value of $\mathrm{d}x/\mathrm{d}t$. Figure 17, on the other hand, shows that the theoretical curves move to the *left* (a little) as St decreases, representing a smaller value. This is emphasized by Figure 18, in which the $St = 0.021$ results from figure 17 are compared with the data from run 31 ($St = 0.019$). Also included in figure 18 are the theoretical and experimental curves for run 48, with the larger amplitude $\epsilon = 0.57$ ($St = 0.021$, $\alpha = 7.0$, $\epsilon_1 = 49$). The theoretical curves are not in agreement with the observation that the waves occur further downstream at the larger amplitude (figure 11). Indeed, additional numerical results predict that the positions of the waves change very little, although their amplitudes are somewhat reduced, as ϵ_1 is increased from 0 to 100, with α fixed; this is equivalent to varying the amplitude ϵ while St is held fixed.

In figure 19, $A(x, t)$ curves are plotted for the case where $g(t)$ is replaced by the first term of its expansion in powers of t, $\pi^2 t^2$; parameter values are chosen to correspond with run 10 (figures 14, 16*a*): $\epsilon_1 = 16.6, \alpha = 5.0$. It can be seen that the wave-generation process is not dependent upon the oscillatory form of $g(t)$, since here the piston accelerates into the channel (and through the other side for $t > 0.521$) for all time. The positions of wave crests are very little affected for t up to 0.2, although they propagate less rapidly downstream for later times; this is illustrated by the broken curves in figure 16(*a*).

3.3. *Boundary layers and separation*

One apparent defect in the theory of §3.1 is the fact that the expansion for u in (11) is not uniformly convergent near the walls, since the leading term tends to zero as y tends to 0 or 1 and the second term does not. Therefore there are critical layers,

of thickness $O(\epsilon)$, at the walls. However, as Smith & Duck (1980) showed for the steady case, the leading, $O(\epsilon)$, term for u in either critical layer is given identically by the appropriate limit of the core solution (11), and hence the critical layers are not important at this order. Considering the plane wall $y = 1$, for example, and setting $\tilde{z} = (1-y)/\epsilon$, $u = \epsilon\tilde{u}$, $v = -\epsilon^2\tilde{v}$, $p = \epsilon^2\tilde{P}(x,t)$, we obtain

$$\left.\begin{aligned} \tilde{u} &= 6(\tilde{z}-A)+O(\epsilon\log\epsilon), \quad \tilde{P} = P+\frac{36}{\epsilon_1}A_{xx}+O(\epsilon), \\ \tilde{v} &= 6A_x(\tilde{z}-A)+\frac{3}{\epsilon_1}A_t-\frac{6}{\epsilon_1}A_{xxx}-\tfrac{1}{6}P_x+O(\epsilon\log\epsilon), \end{aligned}\right\} \tag{22}$$

where the $\log\epsilon$ terms arise because the solution of (7) and (13) for u_2 in the core involves a term that is logarithmically singular as y tends to 0 or 1 (note that the kinematic boundary condition can still be applied on v_2 because $v_2 = O[(1-y)\log(1-y)]$ as $y \to 1$).

We now consider the viscous boundary layers on the walls, which are required because the perturbations to u in (11) do not satisfy the no-slip condition. If a scale for viscous-layer thickness (on either wall) is $a\delta$, a balance between the viscous term and the unsteady inertia term in the x-momentum equation (8) gives

$$\delta^2 = \left[\frac{\epsilon_1}{3\epsilon}\right]^{\frac{3}{4}} 10^{-\frac{1}{4}} Re^{-1} = St^{-1}Re^{-1} = \frac{\nu T}{a^2} \ll 1. \tag{23}$$

Since $u = O(\epsilon)$ and $\epsilon_1 = O(1)$, the convective inertia terms in (8) have the same order of magnitude as the other terms. The fully interactive problem of Smith (1976*b*) is one in which the viscous-layer thickness and the indentation height are comparable; this case leads to the scaling of (3*b*). Here, however, we are interested in cases for which the viscous layer is much thinner than the critical layer, i.e. $\delta \ll \epsilon$, so we require

$$\epsilon \gg Re^{-\frac{3}{7}}. \tag{24}$$

For the viscous layer on $y = 1$ we introduce new variables: $1-y = \delta z$, $u = \epsilon U$, $v = -\delta\epsilon V$, $p = \epsilon^2\tilde{P}(x,t)$; the pressure gradient on this wall $\tilde{P}_x$ is given by (12) and (16) to be

$$\tilde{P}_x = P_x+\frac{36}{\epsilon_1}A_{xxx} = 36\left(\frac{1}{2\epsilon_1}A_t - AA_x\right).$$

At leading order the following, classical, unsteady boundary-layer problem emerges:

$$\left.\begin{aligned} &U_x+V_z = 0, \\ &U_t+\frac{\epsilon_1}{3}(UU_x+VU_z) = -6A_t+12\epsilon_1 AA_x+U_{zz}, \\ &U = V = 0 \quad \text{on } z = 0, \\ &U \sim -6A(x,t) \quad \text{as } z\to\infty. \end{aligned}\right\} \tag{25}$$

For the boundary layer on the indented wall, we make the Prandtl transformation

$$y-\epsilon F = \delta z, \quad v = \delta\epsilon V+\epsilon uF_x+\frac{3\epsilon^2}{\epsilon_1}F_t,$$

and the same, classical problem emerges, except that

$$U \sim 6(F+A) \quad \text{as } z\to\infty$$

and the pressure-gradient term is correspondingly altered (cf. Smith & Duck (1980) for the steady case).

The problem (25) can in principle be solved for sufficiently small t when $A(x,t)$ is known from integration of (17). A semi-analytical approach is to expand in powers of t: let

$$F(x,t) = f(x)\,g(t) = f(x)\sum_{n-2}^{\infty} a_n t^n, \tag{26}$$

then (17) and (18) give

$$B(x,t) = \sum_{n-3}^{\infty} t^n B_n(x), \tag{27}$$

where

$$\left.\begin{aligned} B_3 &= -\tfrac{1}{6}a_2 f^{(3)}, \quad B_4 = -\tfrac{1}{8}(\tfrac{1}{3}a_2 f^{(6)} + a_3 f^{(3)}), \\ B_5 &= -\tfrac{1}{40}[\tfrac{1}{3}a_2 f^{(9)} + a_3 f^{(6)} + 4a_4 f^{(3)}] + \frac{\epsilon_1 a_2^2}{30}(2f'f^{(3)} + 3ff^{(4)}), \end{aligned}\right\} \tag{28}$$

etc. The solution to the problem (25) can now be written as

$$U = \sum_{n-2}^{\infty} t^n U_n(x,\zeta), \quad \zeta = \frac{z}{2t^{\frac{1}{2}}},$$

where

$$U_{n\zeta\zeta} + 2\zeta U_{n\zeta} - 4nU_n = 24n[-\tfrac{1}{2}a_n f(x) + B_n(x)] + \epsilon_1 R_n(x,\zeta;\epsilon_1), \tag{29}$$

and the function R_n depends nonlinearly on the U_m for $m \leqslant n-3$ ($R_n \equiv 0$ for $n \leqslant 4$). Thus U_n can be written as the sum of terms that are products of known functions of x with functions of ζ that satisfy linear ordinary differential equations; U_n can therefore be determined completely.

In general the solutions of classical unsteady boundary-layer problems break down because a singularity arises in the solution for V after a finite time t_s, at some point where the pressure gradient is adverse. This singularity is associated with breakaway separation of the boundary layer (not to be confused with skin-friction reversal, which first occurs at an earlier time), and has been investigated by Van Dommelen & Shen (1980), Elliott, Cowley & Smith (1983) and Cowley (1983*b*). In the present case, if f is smooth enough for its derivatives to be $O(1)$, and if $\epsilon_1 = O(1)$, we would expect $t_s = O(1)$ too. Thus the function $A(x,t)$ and the boundary layers will begin to develop as predicted above, but the theory will no longer be strictly valid for $t \geqslant t_s$.

However, in the limit $\epsilon_1 \to 0$ (corresponding to either small amplitude or large St, from (15)) the solution to (25) can be written in powers of ϵ_1 before being expanded in powers of t. The leading term satisfies the diffusion equation, and is therefore well-behaved for all time as long as A is well-behaved, which is true for $t < 1$ as shown in §3.2. The nonlinear terms that are responsible for the singularity come in only at $O(\epsilon_1)$. Now with A initially behaving as t^2, the $O(\epsilon_1)$ term starts with t^5 (see (28)), the $O(\epsilon_1^2)$ term starts with t^8, etc. This suggests that $t_s \to \infty$ as $\epsilon_1 \to 0$, the dependence probably taking the form $t_s = O(\epsilon_1^{-\frac{1}{3}})$. Thus, if ϵ_1 is small enough, no singularity is to be expected for $0 < t < 1$, and the inviscid theory is self-consistent for the whole of an oscillation period.

When $f(x)$ is given by (19), with α chosen to model the indentation in our experiments, the x-derivatives of $f(x)$, and hence of A, are large at the ends of the indentation; a strong adverse pressure gradient consequently develops on the downstream slope. Thus breakaway separation will develop there early in the cycle, and presumably leads to the formation of the observed separation bubble A (figure

6). On the plane walls, however, the pressure gradients are less steep (cf. figure 15), and therefore the appearance of closed eddies does not necessarily indicate that breakaway separation has occurred. Alternatively, even if breakaway has occurred, it is a matter of conjecture whether the burst of vorticity that presumably then erupts from the boundary layer into the inviscid core inevitably has a significant influence on the core flow. The eddies may still be described approximately by the boundary layer equations, and in that case the basic physics of the waves would be adequately represented by the inviscid model. Our purely inviscid model could perhaps be improved by incorporating the observed shape of the first separation bubble A into the function $F(x, t)$ and then using the same inviscid model for the downstream wave generation. This would have the effect, in the numerical integration, of reducing the effective value of $\hat{\alpha}$ (and hence α) and of increasing the effective value of x_1. According to the results of §3.2, the wave crests would then move further downstream, at a faster rate, which would make predictions agree somewhat better with experiment (figure 18).

The main conclusion of this subsection is that, as ϵ_1 becomes smaller, the inviscid theory for the core flow remains valid for a longer time in the cycle. This is consistent with the results of §3.2, where it was shown that there is better agreement between theory and experiment for larger values of the Strouhal number.

4. Further discussion

While the theory of §3.1 offers an explanation of the generation and propagation of the waves, it sheds no light on their eventual break-up, especially the eddy-doubling process. This is observed to happen very quickly, but thereafter the pair of eddies remain coherent for some time (figures 5*d–f*). The phenomenon thus resembles a rapid bifurcation from one slowly varying state to another. A possible analogy is with the instability of a free shear layer, which evolves quickly into a row of corotating vortices. Another analogy might be drawn with the Rossby-wave instability analysed by Haynes (1984). In that case a 'cat's-eye' pattern develops in the nonlinear critical layer where the fluid speed equals the Rossby-wave speed. When viscosity is small vorticity is advected with the fluid, so in the cat's eyes, where the streamlines are closed, there is a tendency for the lines of constant vorticity to be twisted up 'like spaghetti on a fork' (M. E. McIntyre, personal remark). If the cat's eyes are long and flat, the flow can be regarded as quasi-parallel, and after a certain time the vorticity distribution will satisfy Rayleigh's necessary condition for instability. Numerical work by Haynes (1984) confirmed the presence of instability, and followed its nonlinear development. A similar mechanism might be anticipated here, with the closed eddies beneath the wave crests acting as the cat's eyes.

A weakness in the interpretation of the eddy-doubling process in terms of rapid hydrodynamic instabilities is that it does not explain the sequence of events leading to the formation of the second vortex. As described in §2.2, the upstream vortex of a pair forms later in the cycle than the first, downstream, vortex, whereas the instability mechanisms would suggest simultaneous formation of the two vortices. A more promising conjecture, suggested by F. T. Smith, is that the formation of the upstream vortex of a pair represents the ejection into the flow of a burst of vorticity originating from the breakaway separation of the boundary layer in an adverse pressure gradient; see also Doligalski & Walker (1984). The evolution of such a burst has yet to be analysed in detail in any context, but one might expect it to take the

form of a single rolled-up vortex. However, much more detailed experimental measurements and fluid-mechanical analysis will be required before the mechanism of eddy doubling is fully understood.

The ultimate breakdown of the wave–vortex system is clearly three-dimensional, as noted in §2.2. Orszag & Patera (1983) have shown that there exist nonlinear neutral or slowly-decaying disturbances to Poiseuille flow, with streamline patterns similar to those observed here (figure 6*d*), which become unstable to a very rapidly growing three-dimensional mode if $Re \geqslant 400$. The transverse wavelength of the fastest-growing mode is of the order of $2a$, consistent with the observed disturbance in figure 7(*d*). The analysis of Orszag & Patera did not reveal an intermediate, two-dimensional, eddy-doubling mode. Further experiments are needed to determine the detailed three-dimensional structure of the flow disturbances in our channel in order to compare it with that proposed by Orszag & Patera.

In the theory and the discussion so far we have assumed that the flow in the centreplane of the channel is approximately two-dimensional until the final breakdown. This assumption is based on the observation that there are no significant transverse velocities or non-uniformities during the wave generation and eddy-doubling processes (figure 7). Nevertheless, the flow in the centreplane may be affected by three-dimensionality at the sidewalls; we had no way of assessing the effect. In their steady-flow experiments, Armaly *et al.* (1983) observed such three-dimensional effects whenever $Re > 400$, but a significant influence on the centreplane velocity profile was not reported until $Re \geqslant 1000$; the quantities that were most sensitive to three-dimensional effects were the lengths of the separated eddies. Bertram & Pedley (1983) also observed three-dimensionality in the primary separation bubble A, where fluid velocities are small compared with those in the core, for steady flow with $Re \geqslant 350$. Sobey (1985) has observed some three-dimensionality in his steady- and unsteady-flow experiments at smaller Re ($\leqslant 150$). A detailed experimental investigation of sidewall effects in unsteady separating flow should be made in the future. Theoretical analysis will be difficult, however, as shown by Cowley's (1983*a*) analysis of the three-dimensional steady-flow problem at small ϵ, using the scaling of Smith (1976*a*).

Future theoretical work should examine the interaction of vorticity waves with elastic boundaries, both because of the original collapsible-tube motivation and because of the potential relevance to aerodynamic flutter. Very few theories of flutter have considered the importance of vorticity in the oncoming flow (but for exceptions see Benjamin 1960; Garrad & Carpenter 1982; Howe 1982). Finally, we should note that vorticity waves may not be generated in fully three-dimensional flow such as that in a deformed circular tube. The cross-channel pressure difference induced by a non-axisymmetric perturbation in the wall of a collapsible tube can be relieved by secondary motions in the boundary layer, and there is *no* core flow displacement at $O(\epsilon)$ (Smith 1976*c*). Thus the above theory cannot be applied, and no great simplification appears to be possible.

The experiments described in this paper were made possible by a research grant from the SERC, for which we are most grateful; KDS is also grateful to the NSF for a US–UK Cooperative Research grant. We owe our thanks to many colleagues, especially to C. D. Bertram for designing much of the apparatus (particularly the moulded-rubber membrane), to C. J. Lawrence for taking and measuring many photographs, to D. Cheesley and D. Lipman for invaluable technical assistance, to

S. J. Cowley, M. E. McIntyre, T. W. Secomb and O. R. Tutty for numerous discussions of the theory, and to F. T. Smith for his illuminating comments and for showing us a copy of Smith & Burggraf (1985) before it was published.

REFERENCES

ARMALY, B. F., DURST, F., PEREIRA, J. C. T. & SCHONUNG, B. 1983 Experimental and theoretical investigation of backward-facing step flow. *J. Fluid Mech.* **127**, 473–496.

BENJAMIN, T. B. 1960 Effects of a flexible boundary on hydrodynamic stability. *J. Fluid Mech.* **9**, 513–532.

BERTRAM, C. D. 1982 Two modes of instability in a thick-walled collapsible tube conveying a flow. *J. Biomech.* **15**, 223–224.

BERTRAM, C. D. & PEDLEY, T. J. 1982 A mathematical model of unsteady collapsible tube behaviour. *J. Biomech.* **15**, 39–50.

BERTRAM, C. D. & PEDLEY, T. J. 1983 Steady and unsteady separation in an approximately two-dimensional indented channel. *J. Fluid Mech.* **130**, 315–345.

BOGDANOVA, E. V. & RYZHOV, O. S. 1983 Free and induced oscillations in Poiseuille flow. *Q. J. Mech. Appl. Maths* **36**, 271–287.

CANCELLI, C. & PEDLEY, T. J. 1985 A separated-flow model for collapsible tube oscillations. *J. Fluid Mech.* **157**, 375–404.

CONRAD, W. A. 1969 Pressure–flow relationships in collapsible tubes. *IEEE Trans. Bio-med. Engng* **BME-16**, 284–295.

COWLEY, S. J. 1983*a* Steady flow through distorted rectangular tubes of large aspect ratio. *Proc. R. Soc. Lond.* A **385**, 107–127.

COWLEY, S. J. 1983*b* Computer extension and analytic continuation of Blasius' expansion for impulsive flow past a circular cylinder. *J. Fluid Mech.* **135**, 389–405.

DOLIGALSKI, T. L. & WALKER, J. D. A. 1984 The boundary layer induced by a convected two-dimensional vortex. *J. Fluid Mech.* **139**, 1–28.

DUCK, P. W. 1985 Laminar flow over unsteady humps: the formation of waves. *J. Fluid Mech.* **160**, 465–498.

ELLIOTT, J. W., COWLEY, S. J. & SMITH, F. T. 1983 Breakdown of boundary layers: (i) on moving surfaces; (ii) in semi-similar unsteady flow; (iii) in fully unsteady flow. *Geophys. Astrophys. Fluid Dyn.* **25**, 77–138.

GARRAD, A. D. & CARPENTER, P. W. 1982 A theoretical investigation of flow induced instabilities in compliant coatings. *J. Sound Vib.* **85**, 483–500.

HAYNES, P. H. 1984 Non-linear Rossby wave critical layers in the stratosphere. Ph.D. dissertation, Cambridge University.

HOWE, M. S. 1982 On the stability of boundary-layer flow over a spring-mounted piston. *J. Fluid Mech.* **125**, 59–73.

KATZ, A. I., CHEN, Y. & MORENO, A. H. 1969 Flow through a collapsible tube. *Biophys. J.* **9**, 1261–1279.

ORSZAG, S. A. & PATERA, A. T. 1983 Secondary instability of wall-bounded shear flows. *J. Fluid Mech.* **128**, 347–385.

PEDLEY, T. J. 1984 Wave phenomena in physiological flows. *IMA J. Appl. Maths* **32**, 267–287.

SAVVIDES, C. N. & GERRARD, J. H. 1984 Numerical analysis of the flow through a corrugated tube with application to arterial prostheses. *J. Fluid Mech.* **138**, 129–160.

SCHLICHTING, H. 1968 *Boundary-Layer Theory*, 6th edn. McGraw-Hill.

SECOMB, T. W. 1979 Flows in tubes and channels with indented and moving walls. Ph.D. dissertation, Cambridge University.

SMITH, F. T. 1976*a*, *b* Flow through constricted or dilated pipes and channels. Parts I and II. *Q. J. Mech. Appl. Maths* **29**, 343–364 and 365–376.

SMITH, F. T. 1976*c* Pipe flows distorted by non-symmetric indentation or branching. *Mathematika* **23**, 62–83.

SMITH, F. T. 1982 On the high Reynolds number theory of laminar flows. *IMA J. Appl. Maths* **28**, 207–281.

SMITH, F. T. & BURGGRAF, O. R. 1985 On the development of large-sized, short-scaled disturbances in boundary layers. *Proc. R. Soc. Lond.* A **399**, 25–55.

SMITH, F. T. & DUCK, P. W. 1980 On the severe non-symmetric constriction, curving or cornering of channel flows. *J. Fluid Mech.* **98**, 727–753.

SOBEY, I. J. 1980 On flow through furrowed channels. Part 1. Calculated flow patterns. *J. Fluid Mech.* **96**, 1–26.

SOBEY, I. J. 1982 Oscillatory flows at intermediate Strouhal number in asymmetric channels. *J. Fluid Mech.* **125**, 359–373.

SOBEY, I. J. 1983 The occurrence of separation in oscillatory flow. *J. Fluid Mech.* **134**, 247–257.

SOBEY, I. J. 1985 Observation of waves during oscillatory channel flow. *J. Fluid Mech.* **151**, 395–426.

STEPHANOFF, K. D., PEDLEY, T. J., LAWRENCE, C. J. & SECOMB, T. W. 1983 Fluid flow along a channel with an asymmetric oscillating constriction. *Nature* **305**, 692–695.

STEPHANOFF, K. D., SOBEY, I. J. & BELLHOUSE, B. J. 1980 On flow through furrowed channels. Part 2. Observed flow patterns. *J. Fluid Mech.* **96**, 27–32.

UR, A. & GORDON, M. 1970 Origin of Korotkoff sounds. *Am. J. Physiol.* **218**, 524–529.

VAN DOMMELEN, L. L. & SHEN, S. F. 1980 The spontaneous generation of the singularity in a separating laminar boundary layer. *J. Comput. Phys.* **38**, 125–140.

VLIEGENTHART, A. C. 1971 On finite-difference methods for the Korteweg–de Vries equation. *J. Engng Maths* **5**, 137–155.